LUND UNIVERSITY

FACULTY OF SCIENCE

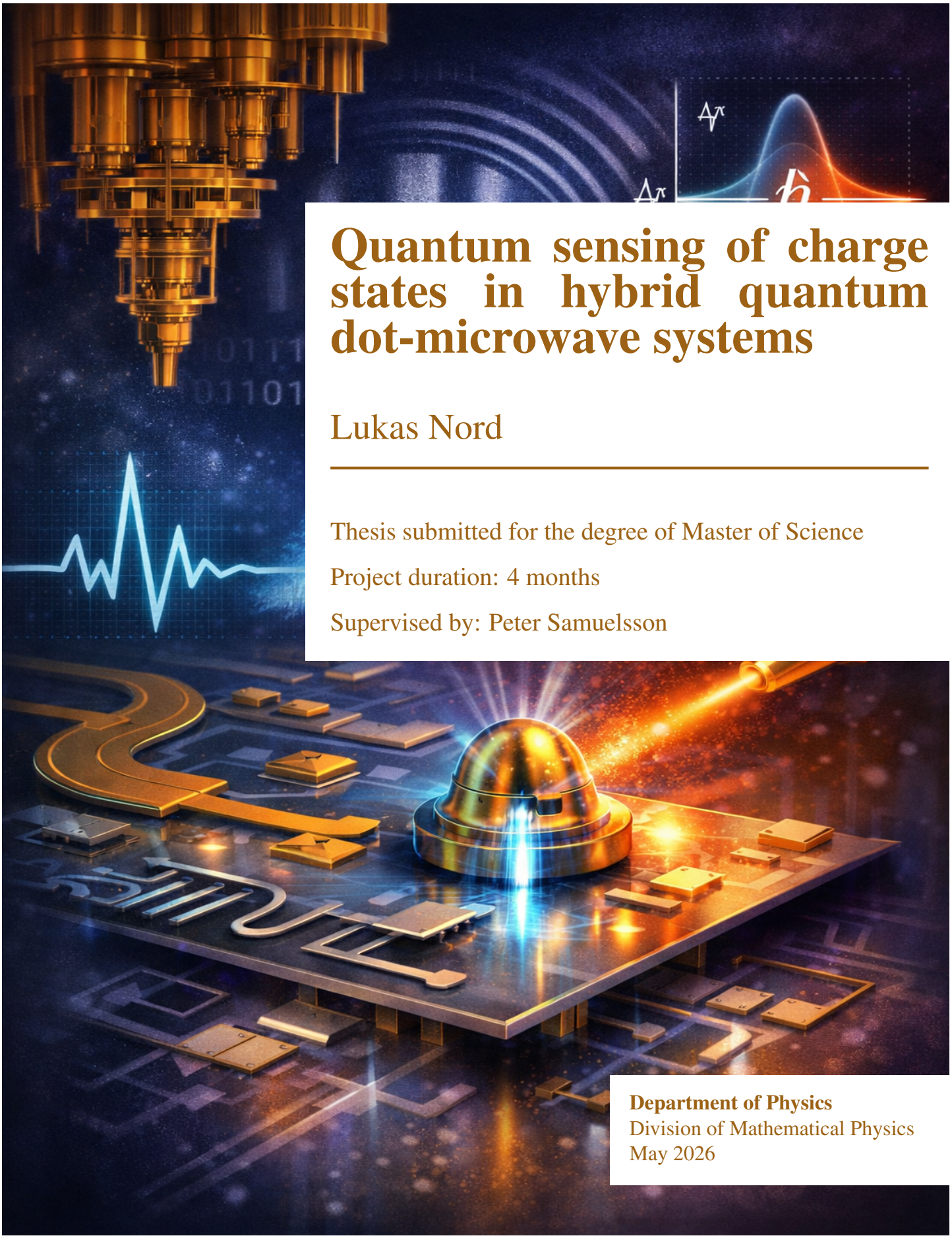

Quantum sensing of charge states in hybrid quantum dot-microwave systems

Lukas Nord

Thesis submitted for the degree of Master of Science

Project duration: 4 months

Supervised by: Peter Samuelsson

Department of Physics
Division of Mathematical Physics
May 2026

[0]Frontpage image generated by chatGPT using prompt "can you generate an image to be used as a front page of a thesis? The topic should be quantum measurements and the quantum limit in circuit quantum electrodynamics. I need it to have as little text as possible and it should be in portrait orientation.".

Abstract

Inspired by the experimental work performed in the research group led by Ville Maisi at Lund University, this thesis investigates a hybrid quantum setup in circuit quantum electrodynamics (cQED). The system consists of a microwave resonator coupled to a double quantum dot (DQD) acting as an internal sensor to indirectly detect the state of an external quantum system. Using input-output theory and quantum Langevin equations, we derive the reflection coefficient of the coupled system, utilizing a mean-field approximation to determine steady-state solutions. The performance and sensitivity of the measurement scheme are quantified using Quantum Fisher Information (QFI) to identify optimal probing regimes for an external system modeled as either a single quantum dot or a secondary two-level qubit. Our results show that the external system induces state-dependent frequency shifts in the sensor qubit, which produce distortions in the reflection spectrum. We find that sensitivity is maximized at probing frequencies corresponding to the steepest slopes of resonance features, in which the reflection is most sensitive to the external system. Ultimately, this work demonstrates that cQED-based hybrid systems provide a versatile platform for indirect state discrimination and provides a foundation for future studies into the quantum limits of sensing.

Acknowledgements

I would like to express my sincere gratitude to the research group led by **Ville Maisi**. Their experimental work served as the primary inspiration for the theoretical models developed in this thesis, providing the physical foundation upon which this study is built. A special thanks is also deserved to **Samuel Andersson**, in said group, for the time he has taken away from his own obligations to support my work. I am also deeply grateful for the guidance and support provided by my supervisor, **Peter Samuelsson**, for the well needed guidence throughout the project.

I want to thank my colleagues in the Department of Mathematical Physics for providing both intellectual inspiration and necessary distractions throughout the writing process. I am profoundly thankful to my partner, **Sandra**, for her unwavering support, as this journey would have been much more difficult without her encouragement. I am also grateful to **my family**, who has supported me, not only through this project, but also through the journey that brought me here. Additionally, I thank the weekly social gatherings at **Pub Rydbergs** for providing much-needed breaks and a space to recharge.

I acknowledge the use of generative AI tools in the preparation of this thesis. These tools were utilized for grammatical refinement and structural improvements, ensuring the clarity and professional flow of the text.

Contents

Acknowledgements **1**

1 Abbreviations and Notations **3**

2 Introduction **4**

3 Quantum Measurements **5**
3.1 Quantum Measurement Strategies 5
3.1.1 Quantum Non-Demolition 5

4 The System **6**
4.1 Definition of a Quantum Dot 6
4.2 Two-Level Double Quantum Dot 7
4.3 The Jaynes-Cummings Hamiltonian 7
4.4 The Combined System 8
4.5 Input Output Relations 9
4.5.1 Heisenberg Equations 9
4.6 Multiple Baths 10
4.7 Lindblad Equation 11

5 The Rotating Frame **11**

6 Reflection Coefficient **12**
6.1 No External System 13
6.1.1 System Dynamics 13

7 Fisher Information **16**
7.1 The Classical Fisher Information 16
7.2 Quantum Fisher Information 16

8 QD as an External System **17**
8.1 System Dynamics 18
8.1.1 Reflection Scanning 19
8.1.2 Fisher Information 24

9 Qubit as an External System **26**
9.1 RWA on the DQD 27
9.2 System Dynamics 28
9.2.1 Reflection Scanning 29
9.2.2 Fisher Information 34

10 Discussion **36**
10.1 Sensitivity and Fisher Information 36
10.2 Comparison between External Systems 36
10.3 Limits of Approximations 37
10.4 Experimental Relevance 37

11 Conclusion **38**
11.1 Outlook 38

References **39**

1 Abbreviations and Notations

cQED: Circuit Quantum Electrodynamics

DQD: Double Quantum Dot

JC: Jaynes-Cummings (referring to the interaction model)

QFI: Quantum Fisher Information

QLE: Quantum Langevin Equation

QND: Quantum Non-Demolition

RWA: Rotating Wave Approximation

SQL: Standard Quantum Limit

ω_r**:** Resonance frequency of the microwave resonator.

ω_q**,** (ω_d)**:** Energy splitting or resonance frequency of the internal sensor qubit (external qubit).

κ**:** Total decay rate of the resonator, representing the sum of all loss processes.

κ_c**:** Coupling decay rate to the transmission line or measurement channel.

Γ_σ**,** (Γ_τ)**:** Decoherence or dissipation rate of the internal sensor qubit (external system qubit).

g**,** (g_d)**:** Coupling strength between the resonator and the sensor qubit (between internal DQD and external system).

$a^\dagger, a$**:** Creation and annihilation operators for the resonator's bosonic mode.

$\sigma_z, \sigma_x, \sigma_y$**:** Pauli operators for the sensor qubit.

$\sigma_\pm$**:** Raising and lowering operators for the sensor qubit.

τ_z, τ_x, τ_y**:** Pauli operators for the external qubit.

$\tau_\pm$**:** Raising and lowering operators for the external qubit.

b_{in}, b_{out}**:** Input and output microwave field operators.

L_k**:** Jump operators used in the Lindblad master equation.

ρ**:** Density matrix of the quantum system.

δ_q**,** (δ_d)**:** Detuning between the site energies of the internal (external) DQD.

t_q**,** (t_d)**:** Tunneling amplitude or tunnel coupling between QDs in the internal (external) DQD.

θ_q**,** (θ_d)**:** Mixing angle used to diagonalize the internal (external) DQD Hamiltonian.

$\Delta_r, \Delta_q, \Delta_d$**:** Detunings relative to the drive frequency ($\omega_r - \omega_{drive}$, $\omega_q - \omega_{drive}$ and $\omega_d - \omega_{drive}$).

$r[\omega]$**:** Reflection coefficient of the microwave signal.

I_q**:** Quantum Fisher Information regarding a parameter of interest.

2 Introduction

Accurate measurement of quantum systems is a central requirement for the development of quantum technologies, including quantum computation, communication, and sensing. Over the past two decades, solid-state architectures, particularly semiconductor quantum dots, have emerged as leading candidates for scalable quantum information processing due to their long coherence times, localized charge states, and compatibility with industrial semiconductor manufacturing frameworks. However, a persistent bottleneck in these platforms is high-fidelity, non-destructive readout. Traditionally, charge states in semiconductor dots were read out using electrometer configurations such as Radio-Frequency Single-Electron Transistors or quantum point contacts. While highly sensitive, these instruments require local galvanically coupled lines, increasing hardware routing footprints and cryogenic thermal dissipation.

To circumvent these structural constraints, the field of Circuit Quantum Electrodynamics (cQED) has adapted techniques originally engineered for superconducting qubits to semiconductor host systems [1, 2]. By embedding semiconductor nanostructures within microwave resonators, researchers can probe internal electronic states through microwave reflection measurements, enabling coherent control and high-fidelity readout [3, 4, 5, 6].

This thesis fits directly into this modern context, establishing a theoretical bridge to recent experimental architectures pioneered in the research group led by Ville Maisi at Lund University. While a major portion of cQED literature emphasizes the direct dispersive sensing of an isolated device [7, 8], this work explores a hybrid architecture where an internal double quantum dot (DQD) acts as an intermediate, auxiliary quantum sensor to indirectly monitor an external target system. In many physical implementations, the target system of interest cannot be accessed directly. By utilizing a secondary DQD system as the sensor, we can achieve high-precision state discrimination while mitigating direct back-action from the probe cavity onto the target environment.

Using input output theory, we derive the reflection coefficient of this coupled hybrid setup and analyze how the measurable cavity response modifies depending on the state of the external system. To quantify the performance of this measurement scheme, we compute the Fisher information associated with the reflected signal [9, 10]. This provides a systematic way to determine the sensitivity of the measurement and to identify the regimes in which small changes in the external system lead to the largest observable effects. Our results demonstrate that the coupling to the external system leads to distinct, measurable shifts in the cavity response that can be reliably used for indirect state discrimination.

The thesis is organized as follows. We begin by introducing the theoretical framework for quantum measurements and relevant measurement strategies in Section 3. In Sections 4, 5, and 6, we present the model of the hybrid system and the formalism used to describe its dynamics. The analysis proceeds from the simplest case of the isolated measurement device (used as an introductory example in Section 6) to progressively more complex scenarios, including coupling to a single-level quantum dot in Section 8, and to a second two-level system in Section 9. Finally, we discuss the results and outline possible directions for future work.

3 Quantum Measurements

Quantum measurement is a fundamental process in physics in which the act of observing a system affects its state. Unlike classical mechanics, where position and momentum can be known simultaneously, quantum objects are described by a wave function that provides probabilistic information about measurement outcomes [2, 11, 12].

When a measurement is performed, the wave function undergoes an irreversible "reduction" or "collapse" to a specific state [11]. Closely related to this is the Heisenberg uncertainty principle, measuring one variable (e.g., position) introduces an unpredictable perturbation to its conjugate variable (e.g., momentum), thereby limiting the precision of subsequent measurements [12, 2]. In addition, all measurements are subject to quantum noise, such as photon shot noise, which limits the measurement rate and causes back-action disturbances on the system [2].

3.1 Quantum Measurement Strategies

There are several types of quantum measurements. In indirect measurements, the measuring device (probe) interacts with the object and then undergoes a separate measurement itself to reveal information about the object. In this case, both the error and the perturbation of the object are linked to the initial uncertainty of the probe's state [11]. Linear measurements involve a continuous or discrete coupling where the back-action is analyzed through the Heisenberg uncertainty relation for perturbation and error [11]. Continuous measurements, unlike discrete measurements that provide a single number, produce a record of a quantity's evolution over time and are often viewed as a sequence of many weak discrete measurements [11].

3.1.1 Quantum Non-Demolition

Traditional measurement schemes are subject to a fundamental precision floor known as the Standard Quantum Limit (SQL). The SQL arises as an unavoidable optimization balance dictated by the Heisenberg Uncertainty Principle when performing continuous linear measurements [2]. For example, in a harmonic oscillator, measuring its position with extreme accuracy increases the uncertainty in its momentum, which subsequently feeds back into the position variance at a later time.

The total measurement error is the sum of two competing quantum noise sources, the intrinsic measurement scale uncertainty (photon shot noise) and the disturbing physical kick given to the system by the meter (measurement back-action). The SQL is formally defined as the minimum absolute noise floor achievable when these two contributions are perfectly balanced. To break past this limit without violating quantum mechanics, specialized measurement protocols must be engineered, which introduces the necessity of Quantum Non-Demolition (QND) measurement frameworks [13, 11, 12]. Their purpose is to overcome the SQL by ensuring that the back-action of the measurement affects only the conjugate (unmeasured) variable [11, 2]. Such measurements are critical for detecting extremely weak signals, such as those from gravitational-wave antennas [12, 11, 13]. An example is the detection of a single photon without destroying it, achieved by using atomic interferometry to measure the phase shift caused by the photon [13].

4 The System

The quantum system considered here consists of a resonator, an internal sensor qubit, and an external system that is to be measured, all seen in figure 1 below. The resonator is modeled as a single bosonic mode with frequency ω_r, coupled to the internal qubit via a Jaynes-Cummings (JC) interaction. The qubit itself is a double quantum dot (DQD) with energy splitting ω_q, with tunable detuning and tunnel coupling. The resonator is coupled to a bosonic bath, modeling the transmission line, described using input-output theory.

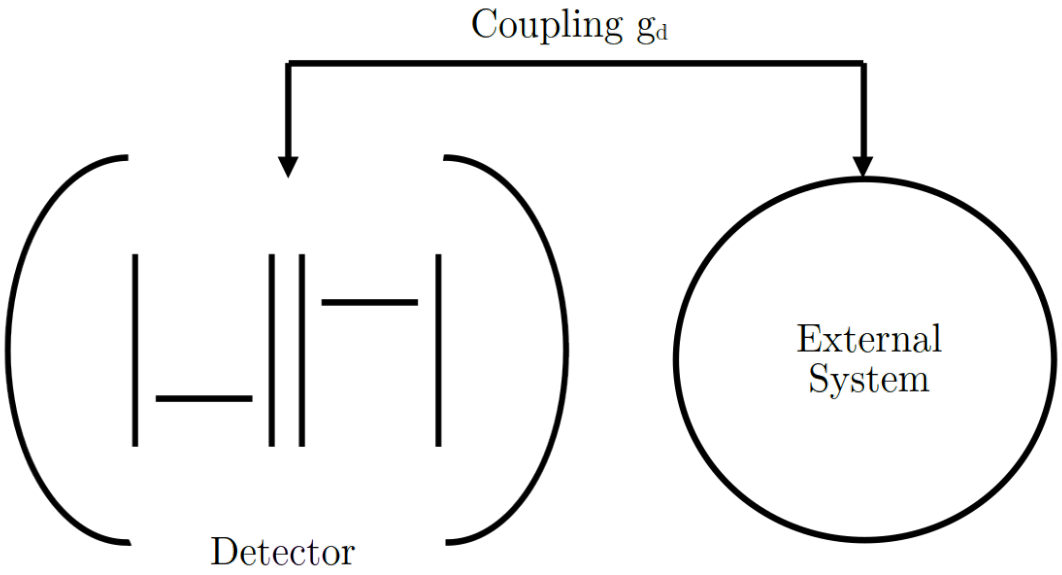

Figure 1: Sketch of the setup, with the sensor, consisting of a DQD in a resonator, to the left, coupled to an external system to the right.

The external system, which is the measurement target, is coupled to the internal sensor qubit. This external system can be modeled either as a single quantum dot with binary occupancy or as a two-level double quantum dot. In both cases, the interaction Hamiltonian couples the state of the external system to the internal qubit, leading to a state-dependent shift in the qubit dynamics. Through its coupling to the resonator, this shift is propagated to the reflected microwave field, allowing indirect readout via the input-output relation.

4.1 Definition of a Quantum Dot

Before analyzing the equations of the coupled system, we explicitly define a quantum dot (QD). A quantum dot is a semiconductor nanostructure that confines charge carriers (such as electrons or holes) in all three spatial dimensions. Because the confinement length scale is comparable to the electron's de Broglie wavelength, the energy spectrum becomes completely discrete, closely resembling the electronic energy shells of an isolated atom. For this reason, quantum dots are frequently referred to as "artificial atoms."

When two such dots are fabricated adjacently, they form a Double Quantum Dot (DQD), where an electron can quantum-mechanically tunnel between the left and right localized potential wells. This architecture forms an effective, highly controllable two-level quantum system (or charge qubit) in the localized basis states $|L\rangle$ and $|R\rangle$ as detailed below.

4.2 Two-Level Double Quantum Dot

The double quantum dot (DQD), acting as our qubit, is defined in a two-level basis representing the left and right quantum dots,

$$|L\rangle = \begin{pmatrix} 1 \\ 0 \end{pmatrix}, \quad |R\rangle = \begin{pmatrix} 0 \\ 1 \end{pmatrix} \tag{4.1}$$

The Hamiltonian for the coupled system, where ε_L and ε_R are the site energies and t is the tunnel coupling, is,

$$H = \varepsilon_L |L\rangle \langle L| + \varepsilon_R |R\rangle \langle R| - t\left(|L\rangle \langle R| + |R\rangle \langle L|\right) = \begin{pmatrix} \varepsilon_L & -t \\ -t & \varepsilon_R \end{pmatrix} \tag{4.2}$$

By defining the detuning, $\delta = \varepsilon_L - \varepsilon_R$, we can diagonalize the Hamiltonian by defining a mixing angle θ and rotating the Hamiltonian by,

$$\tan 2\theta = \frac{2t}{\delta}. \tag{4.3}$$

The Hamiltonian then becomes,

$$H = \frac{1}{2}\omega_q \sigma_z \tag{4.4}$$

The energy eigenstates (ground $|g\rangle$ and excited $|e\rangle$) then become rotations of the localized basis,

$$\begin{pmatrix} |g\rangle \\ |e\rangle \end{pmatrix} = \begin{pmatrix} \cos\frac{\theta}{2} & \sin\frac{\theta}{2} \\ -\sin\frac{\theta}{2} & \cos\frac{\theta}{2} \end{pmatrix} \begin{pmatrix} |L\rangle \\ |R\rangle \end{pmatrix}, \quad \begin{pmatrix} |L\rangle \\ |R\rangle \end{pmatrix} = \begin{pmatrix} \cos\frac{\theta}{2} & -\sin\frac{\theta}{2} \\ \sin\frac{\theta}{2} & \cos\frac{\theta}{2} \end{pmatrix} \begin{pmatrix} |g\rangle \\ |e\rangle \end{pmatrix} \tag{4.5}$$

The Pauli operators, as defined in the localized basis,

$$\tilde{\sigma}_z = |L\rangle \langle L| - |R\rangle \langle R|, \quad \tilde{\sigma}_x = |L\rangle \langle R| + |R\rangle \langle L|, \quad \tilde{\sigma}_y = -i|L\rangle \langle R| + i|R\rangle \langle L|, \tag{4.6}$$

then rotate into the energy basis as,

$$\sigma_z = \cos\theta\, \tilde{\sigma}_z + \sin\theta\, \tilde{\sigma}_x \tag{4.7}$$

$$\sigma_x = \cos\theta\, \tilde{\sigma}_x - \sin\theta\, \tilde{\sigma}_z \tag{4.8}$$

$$\sigma_y = \tilde{\sigma}_y \tag{4.9}$$

where

$$\sigma_z = |e\rangle \langle e| - |g\rangle \langle g|, \quad \sigma_x = |g\rangle \langle e| + |e\rangle \langle g|, \quad \sigma_y = -i|g\rangle \langle e| + i|e\rangle \langle g| \tag{4.10}$$

4.3 The Jaynes-Cummings Hamiltonian

The interaction between the resonator cavity and the internal qubit is described by,

$$H_{\text{rq}} = g(a^\dagger \sigma_- + a\sigma_+), \tag{4.11}$$

which is the Jaynes-Cummings (JC) Hamiltonian [14]. The Jaynes-Cummings model is a framework in quantum optics that describes the coherent interaction between a quantized single-mode electromagnetic field (represented here by the cavity creation and annihilation operators $a^\dagger, a$) and a two-level atom (represented by the Pauli lowering and raising operators $\sigma_\pm$).

In its standard form, it employs the Rotating Wave Approximation (RWA) to neglect highly non-conserving energy terms (such as $a\sigma_-$ and $a^\dagger\sigma_+$), focusing entirely on processes where a photon is absorbed to excite the qubit, or a photon is emitted as the qubit relaxes. In our cQED setup, this Hamiltonian describes the coherent exchange of a single microwave photon between the resonator and the charge states of our internal DQD sensor.

4.4 The Combined System

The complete system we will consider is a combination of those previously described,

$$H = H_r + H_q + H_{rq} + H_{ext} + H_{int} + H_b + H_{sb}, \tag{4.12}$$

where H_r is the Hamiltonian describing the resonator, H_q describes the internal qubit that is coupled to the resonator through the interaction H_{rq}. H_{ext} describes the external system that is to be measured and is coupled to the internal qubit through the interaction H_{int}. The last two terms are the bosonic bath H_b and its interaction with the resonator H_{sb}.

The resonator Hamiltonian is described by,

$$H_r = \omega_r a^\dagger a, \tag{4.13}$$

where the frequency of the resonator is given by ω_r and the creation, $a^\dagger$, and annihilation, a, operators are raising and lowering operators for the mode of the resonator. The Hamiltonian for the internal qubit (q), is,

$$H_q = \frac{1}{2}\omega_q \sigma_z, \tag{4.14}$$

where the frequency $\omega_q = \sqrt{\delta_q^2 + 4t_q^2}$ is related to the difference in energy levels $\delta_q = \varepsilon_L - \varepsilon_R$, and the tunneling amplitude t_q. The interaction between the resonator cavity and the qubit is given by,

$$H_{rq} = g(a^\dagger\sigma_- + a\sigma_+), \tag{4.15}$$

which is the JC Hamiltonian [14]. Here, $\sigma_\pm$ are the raising and lowering operators for the internal qubit. The bosonic bath Hamiltonian is given by [15],

$$H_b = \int_0^\infty d\omega\,\omega b^\dagger(\omega) b(\omega), \tag{4.16}$$

where the b operators are the photon operators, satisfying the commutation relations,

$$\left[b(\omega), b^\dagger(\omega')\right] = \delta(\omega - \omega') \tag{4.17}$$

$$\left[b(\omega), b(\omega')\right] = \left[b^\dagger(\omega), b^\dagger(\omega')\right] = 0. \tag{4.18}$$

The interaction between the cavity and the bath is described by,

$$H_{sb} = i\int_0^\infty d\omega K(\omega)\left[b(\omega) + b^\dagger(\omega)\right]\left[a - a^\dagger\right], \tag{4.19}$$

which simplifies under the rotating wave approximation to,

$$H_{sb} \approx i\int_0^\infty d\omega K(\omega)\left[b^\dagger(\omega)a - a^\dagger b(\omega)\right], \tag{4.20}$$

where, $K(\omega) = \sqrt{\kappa/2\pi}$, following a Markov approximation as described by [15]. This assumption treats the environment as a memoryless reservoir. This holds true because the microwave

transmission line functions as a wide, unstructured continuum. This approximation would fail in structured environments (e.g., photonic crystal waveguides) or in the ultra-strong coupling regime where back-action and memory effects become prominent.

Finally, the external system, H_{ext}, and the coupling to it via the internal qubit, H_{int}, will be modeled as a binary q-dot, that is either occupied or unoccupied, and as an external DQD separately. The full Hamiltonian then becomes,

$$H = \omega_r a^\dagger a + \frac{1}{2}\omega_q \sigma_z + g(a^\dagger \sigma_- + a\sigma_+) \tag{4.21}$$

$$+ \int_0^\infty d\omega\, \omega b^\dagger(\omega) b(\omega) + i \int_0^\infty d\omega \sqrt{\kappa/2\pi} \left[b^\dagger(\omega) a - a^\dagger b(\omega) \right] \tag{4.22}$$

$$+ H_{ext} + H_{int}, \tag{4.23}$$

where the external system is yet to be defined.

4.5 Input Output Relations

Following the methods of [15, 16], we want to investigate how the reflected signal relates to the ingoing signal, and consider the combined Hamiltonian split into three terms,

$$H = H_s + H_{sb} + H_b \tag{4.24}$$

where H_s is the isolated systems Hamiltonian, H_b is the Hamiltonian for the bath and H_{sb} is the interaction between the bath and the system.

We restate the bath Hamiltonian,

$$H_b = \int_0^\infty d\omega\, \omega\, b^\dagger(\omega) b(\omega) \tag{4.25}$$

and the system-bath coupling,

$$H_{sb} = i \int_0^\infty d\omega\, K(\omega) \left[b^\dagger(\omega) a - a^\dagger b(\omega) \right], \tag{4.26}$$

where we consider the approximation,

$$K(\omega) = \sqrt{\frac{\kappa}{2\pi}}. \tag{4.27}$$

4.5.1 Heisenberg Equations

We find the equation of motion for the bath operator, b,

$$\dot{b}(\omega) = -i[b(\omega), H] = -i[b, H_b] - i[b, H_{sb}], \tag{4.28}$$

where we find the commutator with the bath Hamiltonian,

$$[b(\omega), H_b] = \omega b(\omega), \tag{4.29}$$

and with the system-bath coupling,

$$[b(\omega), H_{sb}] = -iK(\omega) a. \tag{4.30}$$

Thus, the equation of motion for the bath operator is,

$$\dot{b}(\omega) = -i\omega b(\omega) + K(\omega)a. \tag{4.31}$$

The formal solution to this differential equation is,

$$b(\omega,t) = e^{-i\omega(t-t_0)}b_0(\omega) + K(\omega)\int_{t_0}^{t} dt' e^{-i\omega(t-t')}a(t'). \tag{4.32}$$

We define the input field as,

$$b_{\text{in}}(t) = \frac{1}{\sqrt{2\pi}}\int d\omega\, e^{-i\omega(t-t_0)}b_0(\omega). \tag{4.33}$$

We now perform the same procedure to an arbitrary operator c,

$$\dot{c} = -i[c,H]\dot{c} = -i[c,H_s] - i[c,H_{sb}] \tag{4.34}$$

where the commutator with the system-bath interaction is,

$$[c,H_{sb}] = i\int d\omega\, K(\omega)\left([c,a]b^\dagger(\omega) - [c,a^\dagger]b(\omega)\right). \tag{4.35}$$

Insert the $b(\omega,t)$ solution, and find the quantum Langevin equation (QLE),

$$\dot{c} = -i[c,H_s] - [c,a^\dagger]\left(\frac{\kappa}{2}a + \sqrt{\kappa}b_{\text{in}}(t)\right) + \left(\frac{\kappa}{2}a^\dagger + \sqrt{\kappa}b_{\text{in}}^\dagger(t)\right)[c,a] \tag{4.36}$$

Similarly, we could define the outgoing field,

$$b_{\text{out}}(t) = \frac{1}{\sqrt{2\pi}}\int d\omega\, e^{-i\omega(t-t_1)}b_1(\omega). \tag{4.37}$$

to find an alternative version of the quantum Langevin equations,

$$\dot{c} = -i[c,H_s] + [c,a^\dagger]\left(\frac{\kappa}{2}a - \sqrt{\kappa}b_{\text{out}}(t)\right) - \left(\frac{\kappa}{2}a^\dagger - \sqrt{\kappa}b_{\text{out}}^\dagger(t)\right)[c,a] \tag{4.38}$$

Comparing the two versions of the equation of motion for the arbitrary operator, equation 4.36 and 4.38, gives the Input-output relation,

$$b_{\text{out}}(t) = b_{\text{in}}(t) + \sqrt{\kappa}a(t) \tag{4.39}$$

4.6 Multiple Baths

If we include multiple baths or decays for the system, these would appear as linear additions to the QLE,

$$\dot{c} = -i[c,H_s] + \sum_k\left[-[c,d_k^\dagger]\left(\frac{\kappa_k}{2}d_k + \sqrt{\kappa_k}b_{\text{in}}^{(k)}(t)\right) + \left(\frac{\kappa_k}{2}d_k^\dagger + \sqrt{\kappa_k}b_{\text{in}}^{\dagger(k)}(t)\right)[c,d_k]\right], \tag{4.40}$$

where the decay operator is d_k, the bath operator is $b_{\text{in}}^{(k)}(t)$ and the decay rate is κ_k for each of the k decay paths.

4.7 Lindblad Equation

We investigate how this formalism relates to the Lindblad formalism. Starting from the multiple bath QLE 4.40, which we can rewrite to,

$$\dot{c} = -i[c,H_s] + \sum_k \left(-[c, \sqrt{\frac{\kappa_k}{2}} d_k^\dagger] \sqrt{\frac{\kappa_k}{2}} d_k + \sqrt{\frac{\kappa_k}{2}} d_k^\dagger [c, \sqrt{\frac{\kappa_k}{2}} d_k] \right) \tag{4.41}$$

$$+ \sum_k \left(-[c, d_k^\dagger] \sqrt{\kappa_k} b_{\text{in}}^{(k)}(t) + \sqrt{\kappa_k} b_{\text{in}}^{\dagger(k)}(t) [c, d_k] \right). \tag{4.42}$$

If we now define the jump operators as $L_k = \sqrt{\kappa_k} d_k$, the equation simplifies to,

$$\dot{c} = -i[c,H_s] + \frac{1}{2} \sum_k \left([L_k^\dagger, c] L_k + L_k^\dagger [c, L_k] \right) + \sum_k \left(-[c, L_k^\dagger] b_{\text{in}}^{(k)}(t) + b_{\text{in}}^{\dagger(k)}(t) [c, L_k] \right). \tag{4.43}$$

Tracing out the bath degrees of freedom removes the explicit input-noise operators, yielding a closed equation for the reduced system evolution,

$$\frac{d}{dt} \langle c \rangle = \left\langle -i[c,H_s] + \frac{1}{2} \sum_k \left([L_k^\dagger, c] L_k + L_k^\dagger [c, L_k] \right) \right\rangle. \tag{4.44}$$

Utilizing that $\frac{d}{dt} \langle c \rangle = \text{tr}(c\dot{\rho})$, and using the cyclic property of the trace, we can find,

$$\dot{\rho} = -i[H_s, \rho] + \sum_k \left(L_k \rho L_k^\dagger - \frac{1}{2} \left\{ L_k^\dagger L_k, \rho \right\} \right), \tag{4.45}$$

which is a Lindblad equation for the system, thus showing that the QLE formalism is equivalent to the Lindblad master equation formalism. Adding a dissipator to the Lindblad equation is then equivalent to adding another term to the sum in the QLE 4.40, with the dissipator operator being the decay operator.

5 The Rotating Frame

To simplify the complexity of the system, we apply the Rotating Wave Approximation (RWA) to this system. This approximation is highly accurate for weak-to-strong coupling regimes where $g \ll \omega_r$. However, it fails if the system enters the ultra-strong coupling regime ($g/\omega_r \gtrsim 0.1$) We transform the laboratory frame Hamiltonian into a rotating frame and eliminate high-frequency oscillating terms.

The Laboratory Frame Hamiltonian is,

$$H = \omega_r a^\dagger a + \frac{1}{2} \omega_q \sigma_z + g(a + a^\dagger)(\sigma_+ + \sigma_-) + H_{drive}(t) + H_{ext} + H_{int} \tag{5.1}$$

Where the resonator is modeled as a single bosonic mode and the qubit is a DQD. The interaction $g(a + a^\dagger)(\sigma_+ + \sigma_-)$ is the Quantum Rabi interaction and becomes the Jaynes-Cummings interaction in the RWA.

To treat the input field as a coherent drive, we replace the input operator $b_{in}(t)$ with its expectation value $b_{in} e^{-i\omega_{drive} t}$. This adds a time-dependent driving term to the Hamiltonian,

$$H_{drive}(t) = \varepsilon (a e^{i\omega_{drive} t} + a^\dagger e^{-i\omega_{drive} t}). \tag{5.2}$$

Here, ε represents the drive strength proportional to the input field amplitude $\sqrt{\kappa}\langle b_{in}\rangle$. We define a unitary transformation $U(t)$ that rotates at the drive frequency ω_{drive},

$$U(t) = \exp\left[i\omega_{drive}t\left(a^\dagger a + \frac{1}{2}\sigma_z + \text{external terms}\right)\right] \tag{5.3}$$

Applying the transformation $H_{rot} = UHU^\dagger + i\dot{U}U^\dagger$ as described in [17], results in,

$$\omega_r \to \omega_r - \omega_{drive} = \Delta_r \tag{5.4}$$
$$\omega_q \to \omega_q - \omega_{drive} = \Delta_q \tag{5.5}$$
$$a \to ae^{-i\omega_{drive}t} \tag{5.6}$$
$$\sigma_- \to \sigma_- e^{-i\omega_{drive}t} \tag{5.7}$$

In the rotating frame, we encounter terms with different phase factors. The stationary terms are terms like $a\sigma_+ e^{-i\omega_{drive}t}e^{i\omega_{drive}t} = a\sigma_+$, and have no time dependence and represent energy-conserving processes. The fast-oscillating terms are terms like $a\sigma_- e^{-i\omega_{drive}t}e^{-i\omega_{drive}t} = a\sigma_- e^{-2i\omega_{drive}t}$, which oscillate at approximately twice the drive frequency. We neglect these fast-oscillating terms, as their net effect averages to zero over the relevant interaction time.

The resulting Hamiltonian in the rotating frame is time-independent and will be used to derive the steady-state dynamics of the system,

$$H_{eff} = \Delta_r a^\dagger a + \frac{1}{2}\Delta_q\sigma_z + g(a^\dagger\sigma_- + a\sigma_+) + \varepsilon(a + a^\dagger) + H_{ext}^{RWA} + H_{int}^{RWA}. \tag{5.8}$$

This effective Hamiltonian is the starting point for deriving the steady-state cavity operator $\langle a\rangle_{ss}$. Any shift in the external system is now reflected as a change in Δ_q, which alters the phase of the reflected signal via the input-output relation $b_{out} = b_{in} + \sqrt{\kappa}a$.

6 Reflection Coefficient

The measurable quantity is the reflected microwave field, determined by the input field and the reflection coefficient. In order to find this coefficient, we consider a system Hamiltonian, and apply the QLE 4.36 to the annihilation operator for the cavity,

$$\dot{a} = -i[a, H_s] + \sum_k \left(-[a, d_k^\dagger]\left(\frac{\kappa_k}{2}d_k + \sqrt{\kappa_k}b_{in}^{(k)}\right) + \left(\frac{\kappa_k}{2}d_k^\dagger + \sqrt{\kappa_k}b_{in}^{\dagger(k)}\right)[a, d_k]\right), \tag{6.1}$$

where d_k are the k decay operators with decay rate κ_k in the system. The QLEs are repeatedly applied to any operator appearing in any equation of motion found. We then find the steady state solutions for these coupled differential equations in the frame rotating at the drive frequency ω_{drive}. This will result in an expression of the form,

$$a[\omega_{drive}] = A[\omega_{drive}]b_{in}[\omega_{drive}] \tag{6.2}$$

Using the input-output relation from equation 4.39, we write,

$$b_{out} = b_{in} + \sqrt{\kappa}Ab_{in} = b_{in}\left(1 + \sqrt{\kappa}A\right). \tag{6.3}$$

The reflection coefficient for this Hamiltonian then becomes,

$$r[\omega] = \frac{\langle b_{out}\rangle}{\langle b_{in}\rangle} = 1 + \kappa A. \tag{6.4}$$

This reflection coefficient describes how the system modifies the incoming field into the reflected field that is to be measured.

6.1 No External System

As an example of calculating the reflection coefficient, we consider the JC-Hamiltonian with no external system,

$$H_{JC} = \omega_r a^\dagger a + \frac{\omega_q}{2}\sigma_z + g(a^\dagger \sigma_- + \sigma_+ a). \tag{6.5}$$

The coupling g is considered weak, such that $g \ll \omega_r, \omega_q$, where ω_r is the resonance frequency of the cavity and ω_q is the resonance frequency of the two-level system. This is in the rotating wave approximation (RWA). a is the annihilation operator for the cavity and σ are the usual Pauli operators.

6.1.1 System Dynamics

We apply the quantum Langevin equation 4.36 to the annihilation operator for the cavity,

$$\dot{a} = -i\omega_r a - ig\sigma_- - \frac{\kappa}{2}a - \sqrt{\kappa_c}b_{in}. \tag{6.6}$$

We see that the σ_- operator has appeared in the equation of motion and therefore also apply the QLE to the σ_- operator, with the dissipator operator, σ_- and decay rate Γ. The qubit is considered otherwise isolated from the environment, and will not interact with an external bath. The equation becomes,

$$\dot{\sigma}_- = -i\omega_q\sigma_- + ig\sigma_z a - \frac{\Gamma}{2}\sigma_-. \tag{6.7}$$

Here, the σ_z operator has appeared. We make the approximation that the drive is weak, such that we can assume that $\sigma_z = -1$. This would mean that the qubit primarily stays in the ground state, and we get,

$$\dot{\sigma}_- = -i\omega_q\sigma_- - iga - \frac{\Gamma}{2}\sigma_-. \tag{6.8}$$

We move into the rotating frame, as described in equation 5.4-5.7, and solve for the steady state,

$$0 = -i\Delta_r a - ig\sigma_- - \frac{\kappa}{2}a - \sqrt{\kappa_c}b_{in} \tag{6.9}$$

$$\sigma_- = -\frac{iga}{i\Delta_q + \frac{\Gamma}{2}}. \tag{6.10}$$

Substituting the Pauli operator equation into the cavity operator equation gives,

$$a[\omega] = \sqrt{\kappa_c}A[\omega]b_{in}[\omega], \tag{6.11}$$

with,

$$A[\omega] = -\frac{\Gamma/2 + i\Delta_q}{(\kappa/2 + i\Delta_r)(\Gamma/2 + i\Delta_q) + g^2}. \tag{6.12}$$

Using the input-output relation from equation 4.39, we can write,

$$b_{out} = b_{in} + \kappa_c A b_{in} = b_{in}\left(1 + \kappa_c A\right). \tag{6.13}$$

The reflection coefficient for the JC Hamiltonian with no external system then becomes,

$$r[\omega] = \frac{\langle b_{out}\rangle}{\langle b_{in}\rangle} = 1 + \kappa_c A \tag{6.14}$$

$$= 1 - \kappa_c \frac{\Gamma/2 + i\Delta_q}{(\kappa/2 + i\Delta_r)(\Gamma/2 + i\Delta_q) + g^2}. \tag{6.15}$$

In figure 2, we see the behaviour of the reflection coefficient. In the right plot, we see two dips, representing the two eigenstates of the coupled qubit-cavity system. On the left, we see how these states are dependent on the probing and qubit frequencies.

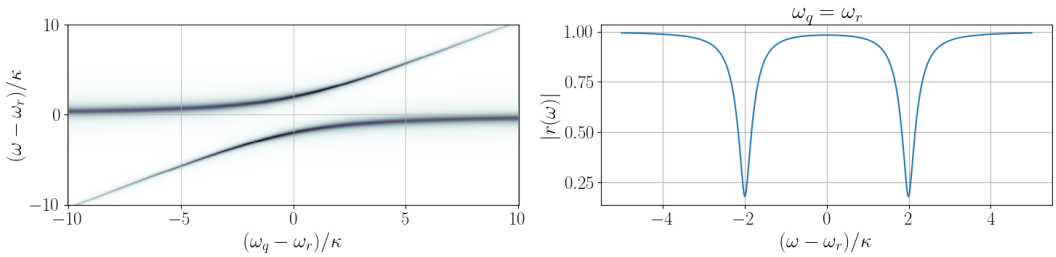

Figure 2: Left: The reflection coefficient is here the intensity of the plot, plotted for a range of frequencies around the cavity resonance frequency, where both the probing and qubit frequency are scanned over. The probing frequency is on the y-axis and the qubit frequency is on the x-axis.
Right: The magnitude of the reflection coefficient, scanned over frequencies near the resonance frequency ω, where ω_r is the bare cavity resonance frequency, ω_q is the sensor qubit transition frequency, and κ represents the cavity decay rate. The qubit is here taken to be on resonance with the cavity.
Plots created with inspiration from [15].

If we instead investigate the effect of the relaxation and the coupling strength, we find figure 3, where we see increasing relaxation rate moving to the right, and increasing coupling strength moving down in the grid.

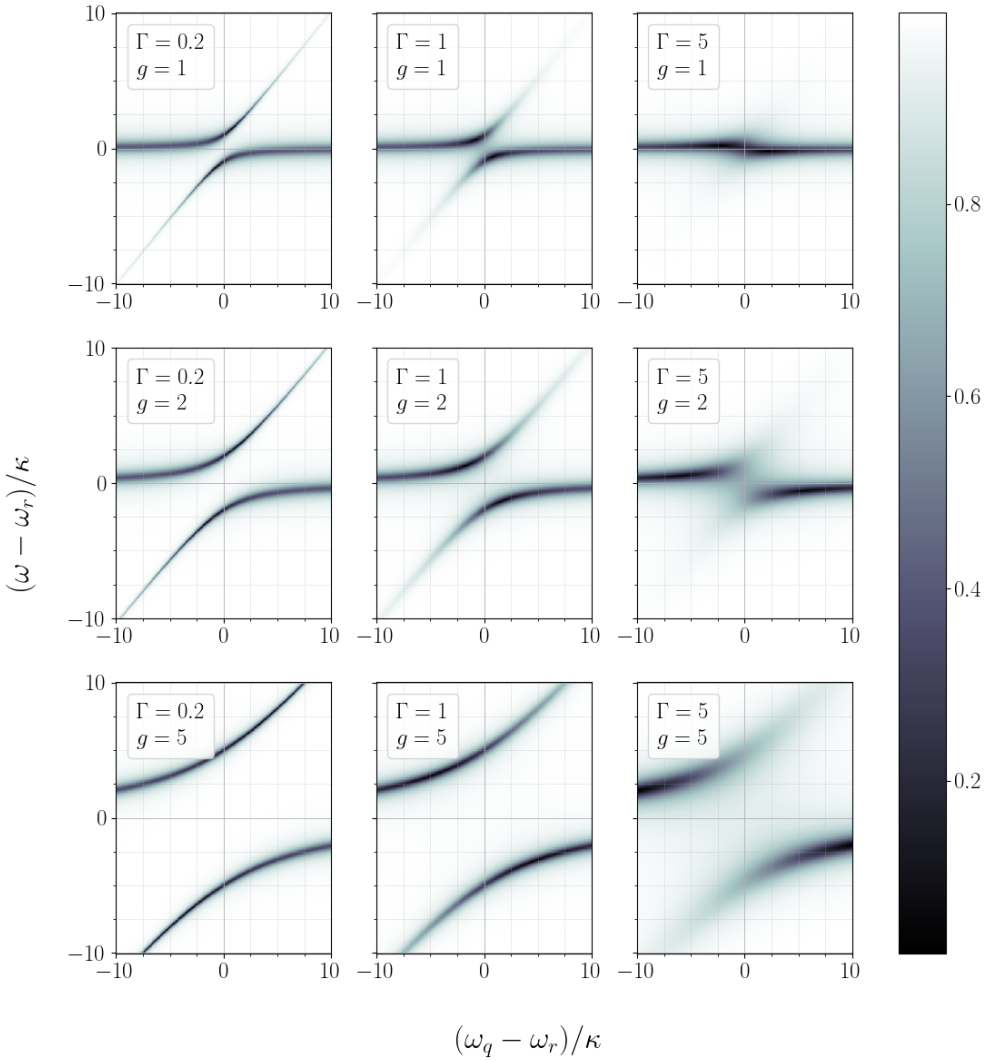

Figure 3: Heatmap of the reflection coefficient for a range of both probing frequencies, ω, and qubit frequencies, Δ_q, around the cavity resonance. The qubit relaxation rate is increasing to the right and the qubit cavity coupling is increasing downwards. Plots created with inspiration from [15].

We see that an increase in the qubit relaxation rate, causes a broadening of the peaks in the reflection, making detailed readout more difficult in such a graph. Increasing the qubit cavity coupling g, we see that the distinction between the two peaks increases. This follows from equation 6.14, from which we expect the poles to be separated by the square of the coupling strength. They are further separated and easier to visually tell apart.

7 Fisher Information

Consider the case where we want to measure one quantity, M, in order to gain information about a parameter θ. We would then assume that there is a relation between them, described by a probability density function $f(x;\theta)$, that generates a distribution for the x values of M for every θ. We then construct an estimator that gives us an estimate for θ for every value x of M.

In this thesis, we consider a coherent probe field and measure the reflected signal $r[\omega]$, which depends on the state of the external system. The goal is to estimate a parameter θ (e.g. occupation or the state of the measured system) from this signal.

7.1 The Classical Fisher Information

Fisher Information measures how much "information" an observable random variable X, such as the reflected microwave signal $r[\omega]$, carries about an unknown parameter θ, for example the position of a particle, or the state of a double quantum dot. It is a measure of sensitivity. The Fisher Information is high if a small change in θ causes a large change in the observable, and vice versa. S.M. Kay [18] presents a lower bound on the variance, σ^2, of any unbiased estimator. This bound is called the Cramér-Rao Lower Bound, and states,

$$\mathrm{Var}(\hat{\theta}) \geq \frac{1}{I(\theta)}, \tag{7.1}$$

where $I(\theta)$ is the Fisher Information presented in [19] as,

$$I(\theta) = \int \left(\frac{\partial}{\partial \theta} \log f(x;\theta) \right)^2 f(x;\theta) dx. \tag{7.2}$$

7.2 Quantum Fisher Information

In the quantum picture, we no longer consider statistical data, but wave functions and density matrices. Nonetheless, one can arrive at a Quantum Cramér-Rao lower bound, as shown by Helström in [20]. It becomes,

$$\mathrm{Var}(\hat{\theta}) \geq \frac{1}{I_q(\theta)}, \tag{7.3}$$

with I_q being the Quantum Fisher information (QFI), defined as,

$$I_q = 4 \sum_{n=1}^{\infty} \left| \langle \phi_n | \frac{\partial \rho}{\partial \theta} | \phi_1 \rangle \right|^2, \tag{7.4}$$

where $|\phi_n\rangle$ are the basis for the density matrix of the system and $|\phi_1\rangle$ is the parameter of interest [20]. In this thesis, all information is gained through the reflected field $\langle b_{out} \rangle$ such that $|\phi_1\rangle = |b_{out}\rangle$. Modelling the input field as a coherent state, with the output field following $b_{out} = r[\omega] b_{in}$, the Fisher information reduces to,

$$I_q = 4 \sum_{n=1}^{\infty} \left| \langle \phi_n | \frac{\partial \rho}{\partial \theta} | b_{out} \rangle \right|^2 = 4 \left| \frac{\partial \langle b_{out} \rangle}{\partial \theta} \right|^2, \tag{7.5}$$

where, θ, is the parameter we want to investigate, such as the occupancy of a q-dot or the state of a qubit. Using the reflection coefficient 6.4, it can instead be written on the form,

$$I_q = 4 |\langle b_{in} \rangle|^2 \left| \frac{\partial r[\omega]}{\partial \theta} \right|^2 = 4 \kappa_c |\langle b_{in} \rangle|^2 \left| \frac{\partial \langle a \rangle_{ss}[\omega]}{\partial \theta} \right|^2. \tag{7.6}$$

8 QD as an External System

In this section, we consider the external system to be a binary q-dot. For a single quantum dot, the Hamiltonian describes a single energy level ε_d that can be either empty or occupied by an electron,

$$H_{ext} = \varepsilon_d |1\rangle\langle 1| \tag{8.1}$$

where $|1\rangle$ is the state where the q-dot is occupied.

The internal sensor qubit can couple with either the left, $|L\rangle$, or the right, $|R\rangle$, q-dot, as seen in figure 4.

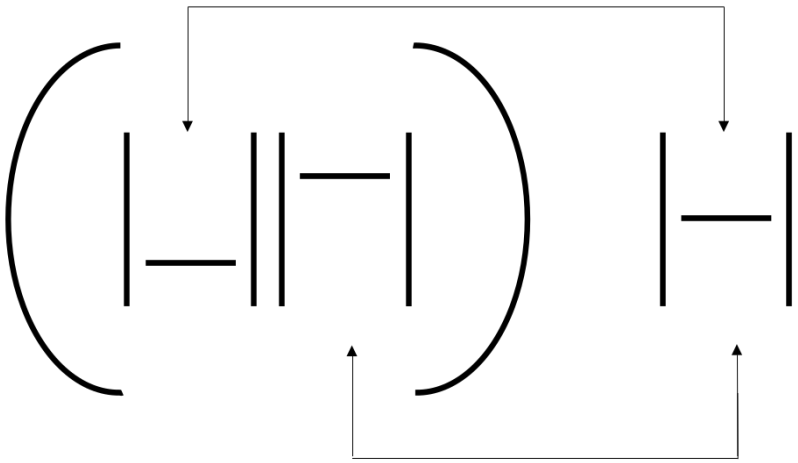

Figure 4: A sketch of the couplings between the different q-dots of the qubit to the external q-dot. The QDs making up the DQD in the cavity on the left, both couple to the external QD on the right.

This interaction is described by the interaction Hamiltonian,

$$H_{int} = g_1 |L\rangle\langle L| \otimes |1\rangle\langle 1| \tag{8.2}$$

$$+ g_2 |R\rangle\langle R| \otimes |1\rangle\langle 1| \tag{8.3}$$

where g_1 and g_2 describe the coupling strength of the capacitive coupling between the q-dot and the left and right side of the sensor qubit. Under the restriction of single electron occupancy in the sensor qubit, we know that $|L\rangle\langle L| = \frac{1}{2}(\mathbb{I} + |L\rangle\langle L| - |R\rangle\langle R|)$ and $|R\rangle\langle R| = \frac{1}{2}(\mathbb{I} - |L\rangle\langle L| + |R\rangle\langle R|)$. Using this, we can rewrite the Hamiltonian into,

$$H_{int} = \mathbb{I} \otimes |1\rangle\langle 1| \left(\frac{g_1 + g_2}{2}\right) \tag{8.4}$$

$$+ (|L\rangle\langle L| - |R\rangle\langle R|) \otimes |1\rangle\langle 1| \left(\frac{g_1 - g_2}{2}\right). \tag{8.5}$$

We want to express this interaction term in the energy basis, rather than the site basis. The rotation uses,

$$\begin{pmatrix} |L\rangle \\ |R\rangle \end{pmatrix} = \begin{pmatrix} cos\theta & sin\theta \\ -sin\theta & cos\theta \end{pmatrix} \begin{pmatrix} |E\rangle \\ |G\rangle \end{pmatrix}, \tag{8.6}$$

where θ is the angle used for rotating the internal qubit. Using this rotation, we find the interaction Hamiltonian in the energy basis,

$$H_{int} = \mathbb{I} \otimes |1\rangle\langle 1| \left(\frac{g_1+g_2}{2}\right) \tag{8.7}$$

$$+ (cos2\theta\sigma_z + sin2\theta\sigma_x) \otimes |1\rangle\langle 1| \left(\frac{g_1-g_2}{2}\right), \tag{8.8}$$

where σ_i are the Pauli operators for the sensor qubit in the energy basis. We can see that the first term act only on the external q-dot, unconditionally, and will only renormalize the q-dot. Therefore, it will be dropped. We also define the coupling $g_d = \frac{g_1-g_2}{2}$, and find the Hamiltonian,

$$H_{int} = (cos2\theta\sigma_z + sin2\theta\sigma_x) \otimes |1\rangle\langle 1| g_d. \tag{8.9}$$

We can define the occupation operator, $n = |1\rangle\langle 1|$, that is here limited to either 1 or 0 electrons. Rewriting the interaction Hamiltonian using this notation, we find,

$$H_{int} = g_d cos2\theta\sigma_z \otimes n + g_d sin2\theta\sigma_x \otimes n. \tag{8.10}$$

In the RWA, this interaction Hamiltonian reduces to,

$$H_{int} = g_d cos2\theta\sigma_z \otimes n. \tag{8.11}$$

We see here, that the resonance frequency will be modified by the state σ_z conditionally on the occupation n.

8.1 System Dynamics

In this system we include relaxation of the qubit using the dissipation operator σ_- with decay rate Γ_σ, as well as the cavity dissipation operator a with decay rate κ. The coupling rate to the transmission line is κ_c. We investigate the dynamics of the system by applying the quantum Langevin equation 4.36 to the cavity operator of this system,

$$\dot{a} = -\frac{a\kappa}{2} - ia\omega_r - \sqrt{\kappa_c} b_{in} - ig\sigma_-, \tag{8.12}$$

and to the qubit lowering operator,

$$\dot{\sigma}_- = -\frac{1}{2}\sigma_-\Gamma_\sigma - i\left(-ag\sigma_z + 2n\sigma_- g_d \cos(2\theta) + \sigma_-\omega_q\right) \tag{8.13}$$

and finally to the σ_z operator,

$$\dot{\sigma}_z = 2i\left(g\left(\sigma_- a^\dagger - a\sigma_+\right)\right) - \Gamma_\sigma(\sigma_z + 1). \tag{8.14}$$

We move these coupled differential equations into an expectation value picture,

$$\langle\dot{a}\rangle = -i\omega_r\langle a\rangle - ig\langle\sigma_-\rangle - \frac{\kappa}{2}\langle a\rangle - \sqrt{\kappa_c} b_{\text{in}} \tag{8.15}$$

$$\langle\dot{\sigma_-}\rangle = -\frac{1}{2}\langle\sigma_-\rangle\Gamma_\sigma - i\left(-g\langle a\sigma_z\rangle + 2n\langle\sigma_-\rangle g_d\cos(2\theta) + \langle\sigma_-\rangle\omega_q\right) \tag{8.16}$$

$$\langle\dot{\sigma}\rangle_z = 2i\left(g(\left\langle a^\dagger\sigma_-\right\rangle - \langle a\sigma_+\rangle)\right) - \Gamma_\sigma(\langle\sigma_z\rangle + 1) \tag{8.17}$$

This reveals a hierarchy of non-linear expectation values, where an increasing number of expansions would be necessary to fully solve the system. We choose to truncate the hierarchy by applying a mean-field approximation, $\langle AB\rangle \approx \langle A\rangle \langle B\rangle$, and look for the steady state solutions in the rotating frame. This approximation neglects entanglement effects and correlations between the subsystems, and is valid when these are small. Solving for these, we find,

$$\langle a\rangle_{ss} = \frac{\sqrt{\kappa_c} b_{in}}{\frac{-2g^2\langle\sigma_z\rangle}{\Gamma_\sigma + 4ing_d\cos(2\theta)+2i\Delta_q} + \frac{\kappa}{2} + i\Delta_r}, \tag{8.18}$$

with the restriction that the steady state must satisfy,

$$\langle\sigma_-\rangle = \frac{2i\langle\sigma_z\rangle\langle a\rangle g}{\Gamma_\sigma + 4ing_d\cos(2\theta) + 2i\omega_q} \tag{8.19}$$

$$0 = 2i\left(g(\left\langle a^\dagger\right\rangle\langle\sigma_-\rangle - \langle a\rangle\langle\sigma_+\rangle)\right) - \Gamma_\sigma(\langle\sigma_z\rangle + 1). \tag{8.20}$$

If we introduce the frequency shift caused by the external system, $\chi(n) = \Delta_q + 2ng_d\cos(2\theta)$, and consider the weak drive limit, where $\langle\sigma_z\rangle \approx -1$, the solutions simplify to the form,

$$\langle a\rangle_{ss} = \frac{\sqrt{\kappa_c} b_{in}}{\frac{2g^2}{\Gamma_\sigma + 2i\chi(n)} + \frac{\kappa}{2} + i\Delta_r}. \tag{8.21}$$

We see here that if we decouple the q-dot from the system, $g_d = 0$, or we have the q-dot be unoccupied, $n = 0$, this reduces to the case where we only considered the JC-Hamiltonian 6.11. The same is also true if the mixing angle for the internal DQD is such that $\cos(2\theta) = 0$. The occupation operator n, is here treated as a free variable, and has no equation of motion. We find the reflection coefficient in this approximation, using the input-output relations 4.39,

$$r[\omega] = 1 - \frac{\sqrt{\kappa_c}\langle a\rangle_{ss}}{b_{in}} = 1 - \frac{\kappa_c\left(\frac{\Gamma_\sigma}{2} + i\chi(n)\right)}{(\frac{\kappa}{2} + i\Delta_r)\left(\frac{\Gamma_\sigma}{2} + i\chi(n)\right) + g^2}. \tag{8.22}$$

8.1.1 Reflection Scanning

We scan this reflection coefficient with probing frequencies ranging from -4κ to 4κ, in the weak drive limit, with the coupling to the transmission line being, $\kappa_c = \frac{1}{2}\kappa$ and with the internal qubit on resonance with the cavity. The light matter coupling between the cavity and the internal qubit is, $g = 2\kappa$, and the coupling between the internal and external qubit and q-dot is, $g_d = 2\kappa$, the relaxation rate for the internal qubit is $\Gamma_\sigma = 1\kappa$, and the tunneling rate in the qubit is $t_q = 0.4\kappa$. These parameters are in units of the total cavity decay rate, κ. This scan generates the reflections seen below for both occupied (orange) and unoccupied (blue) external q-dot.

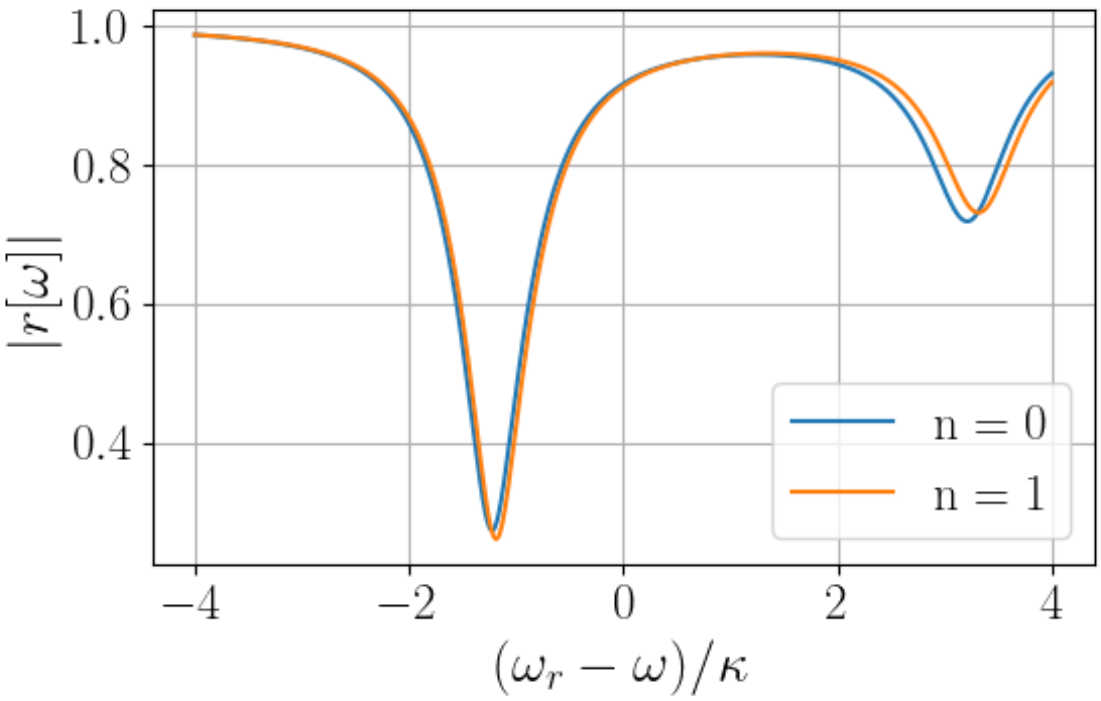

Figure 5: Reflection coefficient $r[\omega]$ as a function of probe frequency for an occupied (orange) and unoccupied (blue) external quantum dot. The x-axis shows the probe detuning relative to the cavity, and the y-axis shows $|r[\omega]|$.
Parameters: $\omega_q = \omega_r$, $g = 2\kappa$, $g_d = 2\kappa$, $\Gamma_\sigma = 1\kappa$, $\kappa_c = 0.5\kappa$.
The presence of the electron shifts the resonance slightly, resulting in distinguishable reflections, which could be used for state discrimination. Whether this is able to be resolved in an experiment, depends on the experimental setup, which will in turn determine the parameter regime.

Here, in figure 5 we can see that the occupancy of the q-dot does shift the position of the peaks in the reflection. This is the effect that should make state discrimination, or the detection of the occupancy, possible. At a given frequency, the magnitude of the reflection has been modified due to the occupancy of the external QD. Since this is barely visible here, these parameters are not optimal for use in state discrimination. The shift caused by $\chi(n) = \Delta_q + 2ng_d\cos(2\theta)$ is not large enough to clearly be visible. Whether this is due to the coupling between the internal DQD and the external QD, g_d, the mixing angle, θ, or the relative position of the resonance peaks is unclear.

In order to investigate how to make the shift large enough to be distinguishable above any experimental background noise, not modeled in this thesis, we choose to se how the reflection behaves if the relative position of the resonance peaks are different. Therefore we move the internal qubit off resonance, $\omega_q \to \omega_q + 1\kappa$, we get the reflections below.

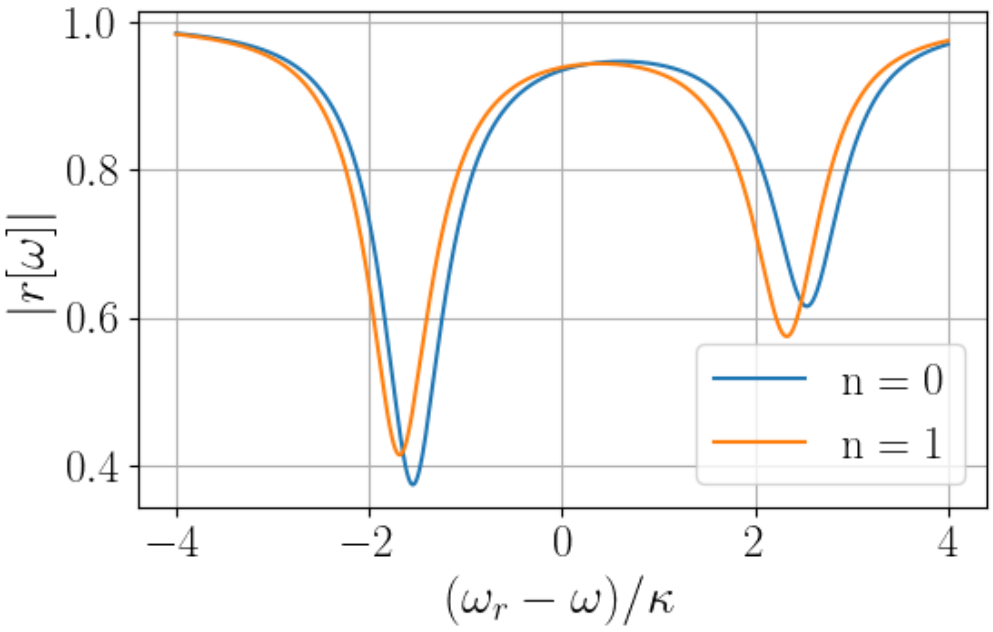

Figure 6: Reflection coefficient $r[\omega]$ as a function of probe frequency for an occupied (orange) and unoccupied (blue) external quantum dot. The x-axis shows the probe detuning relative to the cavity, and the y-axis shows $|r[\omega]|$.
Parameters: $\omega_q = \omega_r + 1\kappa$, $g = 2\kappa$, $g_d = 2\kappa$, $\Gamma_\sigma = 1\kappa$, $\kappa_c = 0.5\kappa$.
With the internal qubit resonance further away from the cavity resonance, the shift caused by the occupancy is now visible. The resonance peaks are shifted in such a way that state discrimination should now be possible using this reflection.

In figure 6, we see the shift caused by the occupancy clearly. The magnitude of the shift has increased due to the offset between the cavity and internal qubit resonances. The peaks in the reflection has been offset due to the occupation of the external q-dot. To see whether this shift becomes clearer when the internal DQD is further into the dispersive regime, we move the resonance, $\omega_q = \omega_r + 1\kappa \to \omega_r + 2\kappa$, and find this reflection coefficient. This yields the reflection below.

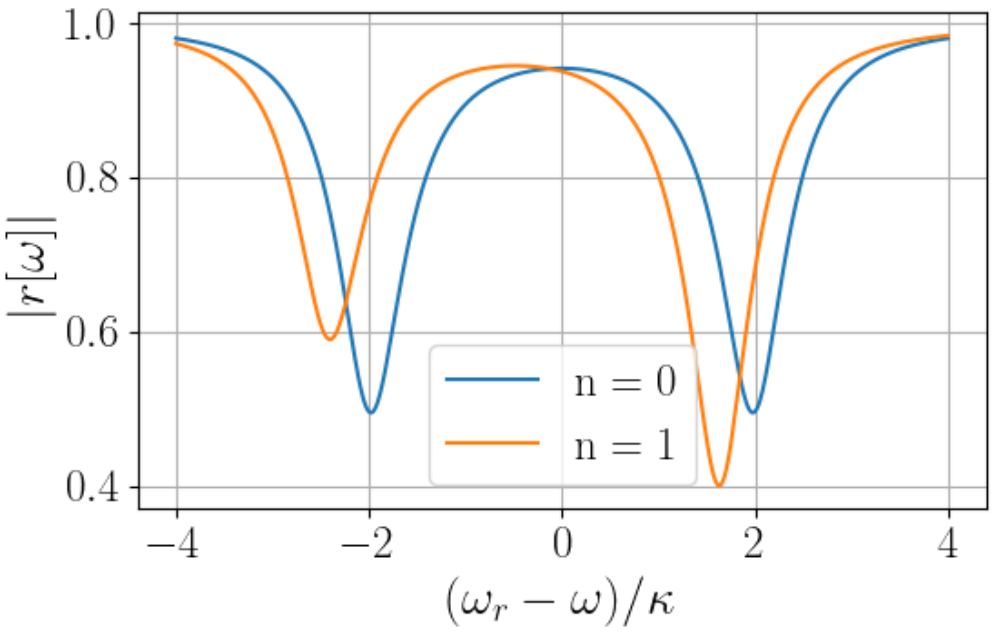

Figure 7: Reflection coefficient $r[\omega]$ as a function of probe frequency for an occupied (orange) and unoccupied (blue) external quantum dot. The x-axis shows the probe detuning relative to the cavity, and the y-axis shows $|r[\omega]|$.
Parameters: $\omega_q = \omega_r + 2\kappa$, $g = 2\kappa$, $g_d = 2\kappa$, $\Gamma_\sigma = 1\kappa$, $\kappa_c = 0.5\kappa$.
The q-dot occupancy shifts the resonance, producing a significant difference in the reflection spectrum. The magnitude of the shift caused by the occupation, has greatly increased. The shift in the external system's state pushes the left mode closer to the sensor qubit's resonance, causing it to inherit more qubit induced decoherence (Γ_σ) and reducing its reflection depth.

In figure 7, we can clearly see that the shift caused by the occupation of the external q-dot, has greatly increased further into the dispersive regime. This leads to the thought that this measurement device would benefit from using frequencies far separated from each other, in the dispersive regime.

Thus far we have only considered the reflection in the weak drive approximation, $\sigma_z \approx -1$. If we want to avoid the use of this approximation, we instead solve the system in equation 8.18 self consistently. We apply the constraints, and get a third order polynomial in σ_z. The zeroes of this polynomial can be found numerically, and these can be used to obtain the steady state of the cavity. These steady states can in turn be used to find the reflection coefficient as seen below.

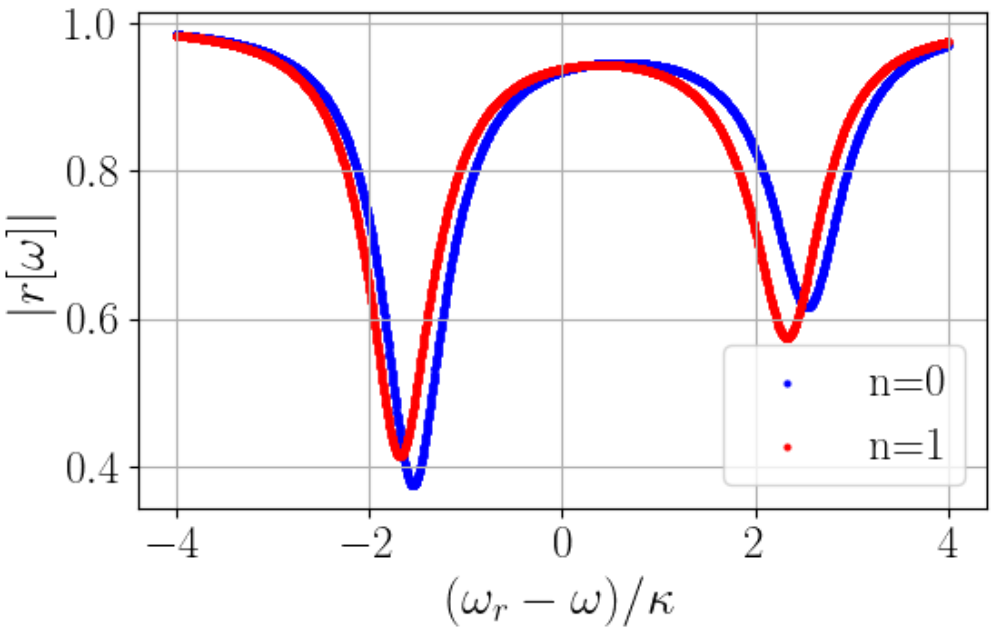

Figure 8: Reflection coefficient $r[\omega]$ as a function of probe frequency for an occupied (red) and unoccupied (blue) external quantum dot. The x-axis shows the probe detuning relative to the cavity, and the y-axis shows $|r[\omega]|$.
Parameters: $\omega_q = \omega_r + 1\kappa$, $g = 2\kappa$, $g_d = 2\kappa$, $\Gamma_\sigma = 1\kappa$, $\kappa_c = 0.5\kappa$.
The electron shifts the resonance, producing a measurable difference in the reflection. We see the same behaviour as in the analytical solution in the weak drive approximation, in figure 6.

We see, in figure 8, that the same pattern as in the previous case occurs. Comparing with figure 6, we see the same result. For these parameters, the weak drive approximation seems to be a good approximation, and we are somewhat justified to further use this approximation. In this case, the numerical approach is feasible, since the equations are only of third order. If the problem becomes more complex, this might not be a possible approach, since the order of the polynomial would then be expected to increase.

Following the analytical approach of increasing the magnitude of the shift in the reflection, we once again choose to investigate the benefit of the dispersive regime in figure 7. We move to the same parameter region, without the weak drive approximation. We then see the reflection seen below.

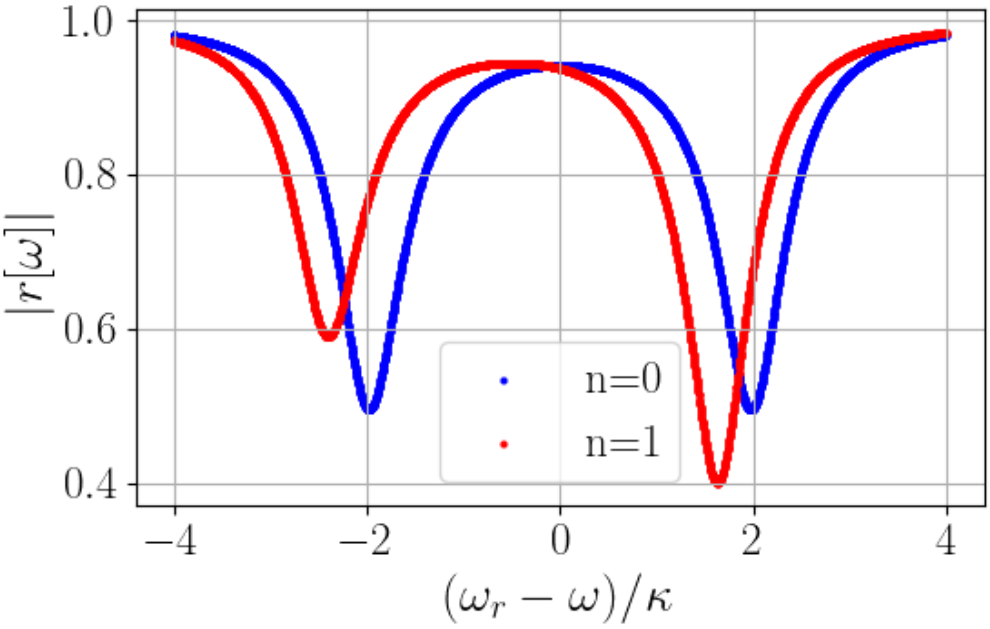

Figure 9: Reflection coefficient $r[\omega]$ as a function of probe frequency for an occupied (red) and unoccupied (blue) external quantum dot. The x-axis shows the probe detuning relative to the cavity, and the y-axis shows $|r[\omega]|$.
Parameters: $\omega_q = \omega_r + 2\kappa$, $g = 2\kappa$, $g_d = 2\kappa$, $\Gamma_\sigma = 1\kappa$, $\kappa_c = 0.5\kappa$.
The same behaviour as in the analytical solution in the weak drive approximation in figure 7 is observed.

In figure 9, we see that the behaviour of figure 7 is not likely affected by the weak drive approximation, since it still pertains without this approximation, further reinforcing the thought of the approximation being good in this parameter regime.

8.1.2 Fisher Information

We now start investigating the limits of what information can be extracted from a reflection coefficient, such as that in equation 8.22. Here we will limit ourselves to the reflection in the weak drive approximation, in which we have a complete analytical expression, with the motivation that the same reflection was obtained even without this approximation. We perform this analysis following equation 7.6, with the parameter we want information about being the binary occupation of the external QD, $\theta = n$. We calculate the response of the cavity steady state on a change in the occupancy of the q-dot,

$$\left|\frac{\partial \langle a\rangle_{ss}}{\partial n}\right|^2 = \frac{4g^2 g_d^2 \left|4ig\sqrt{\kappa_c} b_{in}\cos(2\theta)\right|^2}{\left|2g^2 + \left(\frac{\kappa}{2} + i\Delta_r\right)\left(\Gamma_\sigma + 2i\Delta_q + 4ing_d\cos(2\theta)\right)\right|^4}. \tag{8.23}$$

This is then inserted into equation 7.6 to obtain the QFI, I_q,

$$I_q = 4\kappa_c b_{in}^2 \left|\frac{\partial \langle a\rangle_{ss}}{\partial n}\right|^2. \tag{8.24}$$

This can be maximized in many parameters, but in this paper we consider only the probing frequency, ω, that sits in the detunings, $\Delta_i = \omega_i - \omega$. The Fisher information is shown for a range of probing frequencies, and is accompanied by the respective reflection, in figure 10.

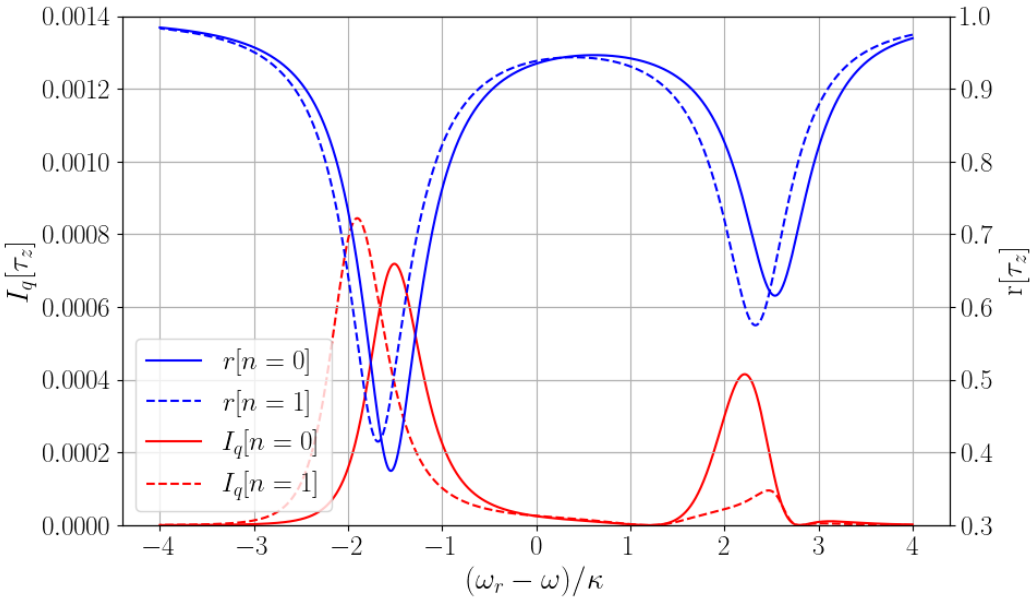

Figure 10: Reflection coefficient $r[\omega]$, and the Fisher information $I_q[\omega]$, as a function of probe frequency for an occupied (right) and unoccupied (left) external quantum dot. The x-axis shows the probe detuning relative to the cavity, and the y-axis shows $|r[\omega]|$ and $I_q[\omega]$ respectively.
Parameters: $\omega_q = \omega_r + 1\kappa$, $g = 2\kappa$, $g_d = 2\kappa$, $\Gamma_\sigma = 1\kappa$, $\kappa_c = 0.5\kappa$.
The QFI peaks around the point in the reflection where the occupation of the external q-bit has the greatest impact on the reflected signal.

We can see, in figure 10, the QFI for a scan of the reflection coefficient with probing frequencies ranging from -4 to 4, the coupling to the transmission line, $\kappa_c = \frac{1}{2}$ and with the internal qubit off resonance with the cavity, $\omega_q = \omega_r + 1$. The light matter coupling between the cavity and the internal qubit is, $g = 2\kappa$, and the coupling between the internal qubit and external q-dot is, $g_d = 2\kappa$, the relaxation rate for the internal qubit is $\Gamma_\sigma = 1\kappa$, and the tunneling rate in the qubit is $t_q = 0.4\kappa$. These parameters are in units of the total cavity decay rate, κ. For unoccupied q-dot in solid lines, and for occupied in dashed lines. The reflection is depicted in blue, and the QFI in red. It can be seen that the QFI is at the maximum in the area around the peaks of the reflections, where it changes the most based on the state of the external system. This means that the reflection is most sensitive to small changes in the occupation of the q-dot at probing frequencies just outside the reflection peaks, in this case. This is not a given, since the derivative in the calculation of the QFI is taken with respect to the occupation, and not the probing frequency.

9 Qubit as an External System

In this section, we consider a qubit, consisting of a double quantum dot, as the external system to be measured on. This qubit is modeled in the same way as the internal qubit, but with its own resonance frequency and tunneling rate.

Using a DQD as the external system, we get an interaction term that couples each of the q-dots of the two qubits to each other, as seen in figure 11.

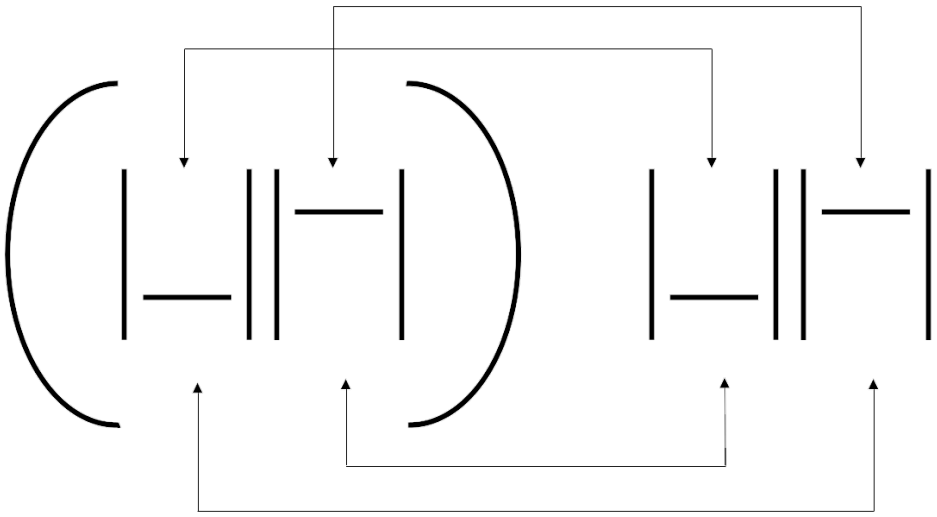

Figure 11: A sketch of the couplings between the different q-dots of the two qubits. The QDs making up the DQD in the cavity on the left, both couple to each of the QDs making up the external DQD on the right.

The interaction term will look like,

$$\begin{aligned} H_{int} =& h_1 |l\rangle \langle l| \otimes |L\rangle \langle L| && (9.1)\\ &+ h_2 |l\rangle \langle l| \otimes |R\rangle \langle R| && (9.2)\\ &+ h_3 |r\rangle \langle r| \otimes |L\rangle \langle L| && (9.3)\\ &+ h_4 |r\rangle \langle r| \otimes |R\rangle \langle R| . && (9.4) \end{aligned}$$

Where we denote the left and right occupation states with $|L\rangle$ and $|R\rangle$ for the external qubit, and similarly using lowercase letters for the internal qubit. By imposing the condition that the qubits will always be occupied by one electron each, we can define the operator,

$$\Delta n_q = |l\rangle \langle l| - |r\rangle \langle r| \qquad \Delta n_d = |L\rangle \langle L| - |R\rangle \langle R| , \tag{9.5}$$

to rewrite the interaction as,

$$H_{int} = \Delta n_d \otimes \Delta n_q \frac{h_1 - h_2 - h_3 + h_4}{4} \tag{9.6}$$

$$+ \Delta n_d \otimes \mathbb{I} \frac{h_1 + h_2 - h_3 - h_4}{4} \tag{9.7}$$

$$+ \mathbb{I} \otimes \Delta n_q \frac{h_1 - h_2 + h_3 - h_4}{4} \tag{9.8}$$

$$+ \mathbb{I} \otimes \mathbb{I} \frac{h_1 + h_2 + h_3 + h_4}{4}. \tag{9.9}$$

We want to express this interaction term in the energy basis, rather than the site basis. The rotation for this uses,

$$\begin{pmatrix} |L\rangle \\ |R\rangle \end{pmatrix} = \begin{pmatrix} cos\theta_d & sin\theta_d \\ -sin\theta_d & cos\theta_d \end{pmatrix} \begin{pmatrix} |E\rangle \\ |G\rangle \end{pmatrix}, \qquad \begin{pmatrix} |l\rangle \\ |r\rangle \end{pmatrix} = \begin{pmatrix} cos\theta_q & sin\theta_q \\ -sin\theta_q & cos\theta_q \end{pmatrix} \begin{pmatrix} |e\rangle \\ |g\rangle \end{pmatrix}, \tag{9.10}$$

where θ_d and θ_q, defined as $\tan 2\theta_{d/q} = \frac{2t_{d/q}}{\delta_{d/q}}$, are the angles used for rotating the external and internal qubits respectively. Using this rotation, we find the interaction Hamiltonian in the energy basis,

$$H_{int} = (cos2\theta_d \tau_z + sin2\theta_d \tau_x) \otimes \left(cos2\theta_q \sigma_z + sin2\theta_q \sigma_x\right) \frac{h_1 - h_2 - h_3 + h_4}{4} \tag{9.11}$$

$$+ (cos2\theta_d \tau_z + sin2\theta_d \tau_x) \otimes \mathbb{I} \frac{h_1 + h_2 - h_3 - h_4}{4} \tag{9.12}$$

$$+ \mathbb{I} \otimes \left(cos2\theta_q \sigma_z + sin2\theta_q \sigma_x\right) \frac{h_1 - h_2 + h_3 - h_4}{4} \tag{9.13}$$

$$+ \mathbb{I} \otimes \mathbb{I} \frac{h_1 + h_2 + h_3 + h_4}{4}, \tag{9.14}$$

where σ_z, σ_x and τ_z, τ_x are Pauli operators acting on the internal and external qubit respectively. We can now note that the last term simply shifts the energies, thus this term will be dropped, and the second and third terms acts only locally and can be absorbed into the local qubit Hamiltonians. Thus, the simplified Hamiltonian becomes,

$$H_{int} = (cos2\theta_d \tau_z + sin2\theta_d \tau_x) \otimes \left(cos2\theta_q \sigma_z + sin2\theta_q \sigma_x\right) g_d, \tag{9.15}$$

with the coupling defined as $g_d = \frac{h_1 - h_2 - h_3 + h_4}{4}$.

9.1 RWA on the DQD

In order to simplify the cross-terms of the interaction between the two qubits, we first move the external qubit into the rotating frame, in which we work, and find that,

$$\omega_r \to \omega_r - \omega_{drive} = \Delta_r \tag{9.16}$$

$$\omega_d \to \omega_d - \omega_{drive} = \Delta_d \quad \omega_q \to \quad \omega_q - \omega_{drive} = \Delta_q \tag{9.17}$$

$$a \to a e^{-i\omega_{drive} t} \tag{9.18}$$

$$\tau_- \to \tau_- e^{-i\omega_{drive} t} \quad \sigma_- \to \quad \sigma_- e^{-i\omega_{drive} t} \tag{9.19}$$

With all parts in the rotating frame, we want to simplify the interaction Hamiltonian. Using that $\tau_x = \tau_- + \tau_+$ and $\tau_+ = \tau_-^\dagger$, we expand and substitute into the Hamiltonian.

$$
\begin{aligned}
H_{int} =& g_d \cos(2\theta_d)\cos\big(2\theta_q\big)\tau_z\sigma_z && (9.20)\\
&+ g_d \cos(2\theta_d)\sin\big(2\theta_q\big)\tau_z(\sigma_- e^{-i\omega_{drive}t} + \sigma_+ e^{i\omega_{drive}t}) && (9.21)\\
&+ g_d \sin(2\theta_d)\cos\big(2\theta_q\big)(\tau_- e^{-i\omega_{drive}t} + \tau_+ e^{i\omega_{drive}t})\sigma_z && (9.22)\\
&+ g_d \sin(2\theta_d)\sin\big(2\theta_q\big)(\tau_- e^{-i\omega_{drive}t} + \tau_+ e^{i\omega_{drive}t})(\sigma_- e^{-i\omega_{drive}t} + \sigma_+ e^{i\omega_{drive}t}) && (9.23)
\end{aligned}
$$

Applying the rotating wave approximation, by neglecting any terms that do not become time-independent in the rotating frame, we arrive at,

$$
\begin{aligned}
H_{int}^{RWA} =& g_d \Big[\cos(2\theta_d)\cos\big(2\theta_q\big)(\tau_z\sigma_z) && (9.24)\\
&+ \sin(2\theta_d)\sin\big(2\theta_q\big)(\tau_+\sigma_- + \tau_-\sigma_+)\Big]. && (9.25)
\end{aligned}
$$

This is the interaction term between the two qubits, in the rotating wave approximation, which will be used from here on.

9.2 System Dynamics

We now start to investigate how the system evolves over time. For visibility, we define the objects $C = \cos\big(2\theta_q\big)\cos(2\theta_d)$, and $S = \sin\big(2\theta_q\big)\sin(2\theta_d)$, as well as, $B = \sin(2\theta_d)\sin\big(2\theta_q\big)$ and apply the Langevin equation 4.36, to all of the system operators,

$$
\begin{cases}
\dot{a} &= -i\,(a\omega_r + g\sigma_-) - \frac{a\kappa}{2} - \sqrt{\kappa_c}b_{in}\\
\dot{\sigma_-} &= -\frac{\sigma_-\Gamma_\sigma}{2} + i\left(ga\sigma_z - 2g_dC\tau_z\sigma_- + g_dB\tau_-\sigma_z - \sigma_-\omega_q\right)\\
\dot{\tau_-} &= -\frac{\tau_-\Gamma_\tau}{2} - i\,(2g_dC\tau_-\sigma_z - g_dB\tau_z\sigma_- + \tau_-\omega_d)\\
\dot{\sigma_z} &= -\Gamma_\sigma\,(\sigma_z+1) - i\left(2g\left(a\sigma_+ - a^\dagger\sigma_-\right) + 2g_d\,(\tau_-\sigma_+ - \tau_+\sigma_-)\,S\right)\\
\dot{\tau_z} &= -\Gamma_\tau\,(\tau_z+1) + 2ig_d\,(\tau_-\sigma_+ - \tau_+\sigma_-)\,S
\end{cases}
$$

This results in five non-linear coupled operator-valued differential equations. To solve these, we move into the expectation value picture, yielding the following coupled differential equations,

$$
\begin{cases}
\langle\dot{a}\rangle &= -i\,(\langle a\rangle\,\omega_r + g\,\langle\sigma_-\rangle) - \frac{\langle a\rangle\kappa}{2} - \sqrt{\kappa_c}b_{in}\\
\langle\dot{\sigma_-}\rangle &= -\frac{\langle\sigma_-\rangle\Gamma_\sigma}{2} + i\left(g\,\langle a\sigma_z\rangle - 2g_dC\,\langle\tau_z\sigma_-\rangle + g_dB\,\langle\tau_-\sigma_z\rangle - \langle\sigma_-\rangle\,\omega_q\right)\\
\langle\dot{\tau_-}\rangle &= -\frac{\langle\tau_-\rangle\Gamma_\tau}{2} - i\,(2g_dC\,\langle\tau_-\sigma_z\rangle - g_dB\,\langle\tau_z\sigma_-\rangle + \langle\tau_-\rangle\,\omega_d)\\
\langle\dot{\sigma_z}\rangle &= -\Gamma_\sigma\,(\langle\sigma_z\rangle+1) - i\left(2g\left(\langle a\sigma_+\rangle - \left\langle a^\dagger\sigma_-\right\rangle\right) + 2g_d\,(\langle\tau_-\sigma_+\rangle - \langle\tau_+\sigma_-\rangle)\,S\right)\\
\langle\dot{\tau_z}\rangle &= -\Gamma_\tau\,(\langle\tau_z\rangle+1) + 2ig_d\,(\langle\tau_-\sigma_+\rangle - \langle\tau_+\sigma_-\rangle)\,S
\end{cases}
$$

Here, we can see a problem of hierarchies. If we were to solve these, the expectation values of the products of operators would require additional equations of motion, and the problem would significantly grow in complexity. This full problem is beyond the scope of this thesis. Instead, we perform a mean-field approximation, such that $\langle AB\rangle = \langle A\rangle\,\langle B\rangle$. This approximation neglects entanglement effects and correlations between the subsystems, and is valid when the system is operated in the weak driving (low-photon) regime, or when the system-target coupling strength (g_d) is significantly smaller than the dissipation rates (κ, Γ_σ) of the cavity and the sensor qubit.

This results in,

$$\begin{cases} \dot{\langle a \rangle} & = -i\left(\langle a \rangle \omega_r + g\langle \sigma_- \rangle\right) - \frac{\langle a \rangle \kappa}{2} - \sqrt{\kappa_c} b_{in} \\ \dot{\langle \sigma_- \rangle} & = -\frac{\langle \sigma_- \rangle \Gamma_\sigma}{2} + i\left(g\langle a \rangle \langle \sigma_z \rangle - 2g_d C \langle \tau_z \rangle \langle \sigma_- \rangle + g_d B \langle \tau_- \rangle \langle \sigma_z \rangle - \langle \sigma_- \rangle \omega_q\right) \\ \dot{\langle \tau_- \rangle} & = -\frac{\langle \tau_- \rangle \Gamma_\tau}{2} - i\left(2g_d C \langle \tau_- \rangle \langle \sigma_z \rangle - g_d B \langle \tau_z \rangle \langle \sigma_- \rangle + \langle \tau_- \rangle \omega_d\right) \\ \dot{\langle \sigma_z \rangle} & = -\Gamma_\sigma\left(\langle \sigma_z \rangle + 1\right) - i\left(2g\left(\langle a \rangle \langle \sigma_+ \rangle - \langle a^\dagger \rangle \langle \sigma_- \rangle\right) + 2g_d\left(\langle \tau_- \rangle \langle \sigma_+ \rangle - \langle \tau_+ \rangle \langle \sigma_- \rangle\right) S\right) \\ \dot{\langle \tau_z \rangle} & = -\Gamma_\tau\left(\langle \tau_z \rangle + 1\right) + 2ig_d\left(\langle \tau_- \rangle \langle \sigma_+ \rangle - \langle \tau_+ \rangle \langle \sigma_- \rangle\right) S. \end{cases}$$

These equations are now solvable, and we can find the steady states in the rotating frame. We then find,

$$\langle a \rangle_{ss} = \frac{\sqrt{\kappa_c} b_{in}\left(\frac{\Gamma_\sigma}{2} + 2ig_d\tau_z\left(C - \frac{g_d\sigma_z S^2}{i\Gamma_\tau + 2\Delta_d + 4g_d\sigma_z C}\right) + i\Delta_q\right)}{-g^2\sigma_z + \left(i\Delta_r + \frac{\kappa}{2}\right)\left(\frac{\Gamma_\sigma}{2} + 2ig_d\tau_z\left(C - \frac{g_d\sigma_z S^2}{i\Gamma_\tau + 2\Delta_d + 4g_d\sigma_z C}\right) + i\Delta_q\right)} \tag{9.26}$$

for the cavity operator. Here, we once again see a shift in the frequency, caused by the state of the external system, by,

$$\chi(\tau_z) = 2g_d\tau_z\left(C - \frac{g_d\sigma_z S^2}{-i\Gamma_\tau + 2\Delta_d + 4g_d\sigma_z C}\right) + \Delta_q \tag{9.27}$$

with which the steady state is,

$$\langle a \rangle_{ss} = \frac{\sqrt{\kappa_c} b_{in}\left(\frac{\Gamma_\sigma}{2} + i\chi(\tau_z)\right)}{-g^2\sigma_z + \left(i\Delta_r + \frac{\kappa}{2}\right)\left(\frac{\Gamma_\sigma}{2} + i\chi(\tau_z)\right)}, \tag{9.28}$$

which has a form similar to those of the previously found steady states of the system coupled to a q-dot and the isolated system.

9.2.1 Reflection Scanning

We scan the reflection of this system coupled to the external qubit, with probing frequencies ranging from -4 to 4, in the weak drive approximation, with the coupling to the transmission line, $\kappa_c = \frac{1}{2}$ and with the internal qubit on resonance with the cavity, but the external off resonance by 2, $\omega_d = \omega_r + 2$. The light matter coupling between the cavity and the internal qubit is, $g = 2\kappa$, and the coupling between the internal and external qubit and q-dot is, $g_d = 0.5\kappa$, the relaxation rate for the internal and external qubit is $\Gamma_\tau = \Gamma_\sigma = 1\kappa$, and the tunneling rate in the qubits are $t_q = t_d = 0.4\kappa$. These parameters are in units of the total cavity decay rate, κ. This scan generates the reflections seen below for both occupied (orange) and unoccupied (blue) external q-dot.

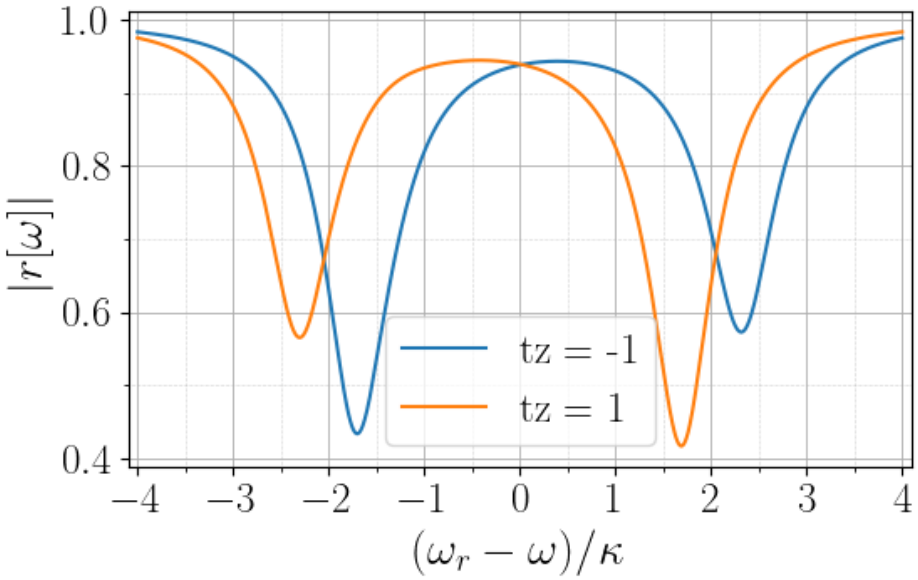

Figure 12: Reflection coefficient $r[\omega]$ as a function of probe frequency for an occupied (orange) and unoccupied (blue) external DQD. The x-axis shows the probe detuning relative to the cavity, and the y-axis shows $|r[\omega]|$.
Parameters: $\omega_q = \omega_r$, $\omega_d = \omega_r + 2\kappa$, $g = 2\kappa$, $g_d = 0.5\kappa$, $\Gamma_\tau = \Gamma_\sigma = 1\kappa$, $\kappa_c = 0.5\kappa$.
The presence of the electron shifts the resonance, producing a difference in the reflection spectrum that enables state discrimination. The reflections for the two states differ most at the resonance frequency of the external system ω_d.

In figure 12, we can see how the state of the external system shifts the resonance of the reflection slightly. This is what could be used for state discrimination.

If we now move the internal qubit off resonance with the cavity, the external qubit could be on resonance with either the cavity or the internal qubit. Both scenarios are visualized below,

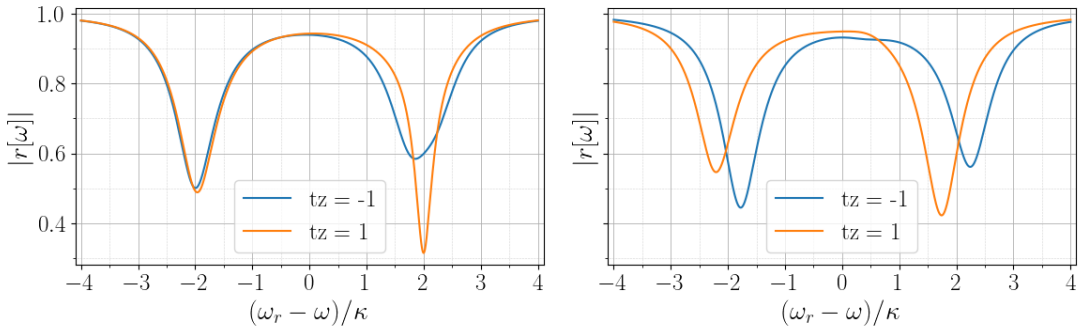

Figure 13: Reflection coefficient $r[\omega]$ as a function of probe frequency for an occupied (orange) and unoccupied (blue) external DQD.
Parameters (left): $\omega_q = \omega_r + 2\kappa$, $\omega_d = \omega_r$
Parameters (right): $\omega_q = \omega_r + 2\kappa$, $\omega_d = \omega_r + 2\kappa$
Parameters (both): $g = 2\kappa$, $g_d = 0.5\kappa$, $\Gamma_\tau = \Gamma_\sigma = 1\kappa$, $\kappa_c = 0.5\kappa$.
The presence of the electron shifts the resonance, producing a measurable difference in the reflection spectrum that enables state discrimination. In the right panel with the external qubit off resonance, it seems to be easier to discriminate the states than in the left pane.

In the case where the external qubit is on resonance with the cavity, seen in the left panel in figure 13, we see that the excited state of the external DQD has slightly shifted the reflection. Through this shift, state discrimination should be possible. In the right panel, we instead see the case where the two DQDs are on resonance with each other, but not with the cavity. Here, we see a larger shift in the reflection, making the state discrimination easier. With the external system on resonance with the cavity, the amplitude of the reflection peak becomes narrower and deeper, while, with the DQD off resonance, the shift in the position of the peak is more apparent.

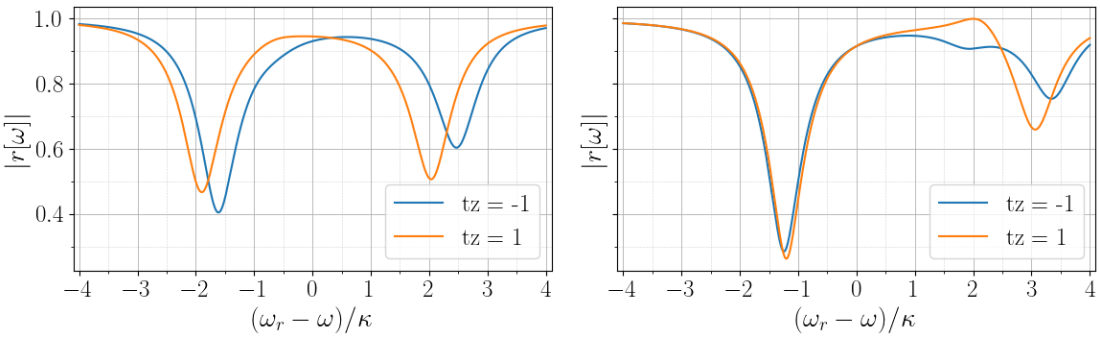

Figure 14: Reflection coefficient $r[\omega]$ as a function of probe frequency for an occupied (orange) and unoccupied (blue) external DQD.
Parameters (left): $\omega_q = \omega_r + 1.5\kappa$, $\omega_d = \omega_r + 3\kappa$
Parameters (right): $\omega_q = \omega_d = \omega_r$
Parameters (both): $g = 2\kappa$, $g_d = 0.5\kappa$, $\Gamma_\tau = \Gamma_\sigma = 1\kappa$, $\kappa_c = 0.5\kappa$.
The presence of the electron shifts the resonance, producing a change in the reflection spectrum that enables state discrimination.

There are still two unexplored situations, in which all three systems (two DQDs and the

cavity) are on resonance with each other, and where they are all off resonance with each other.

In the left panel in figure 14, we observe the three systems off resonance with each other, and wee see almost the same result as in the right panel in figure 13. The external DQD seems to pull the peaks of the reflection to the right by about the same amount, regardless of the position of the resonance for the external DQD, ω_d. In the right pane, we see the case where all three subsystems are on resonance, and comparing to figure 12, we see that changing the position of the external DQD resonance seems to alter the amplitude of the reflection peaks.

We want to observe the behaviour in the case where the weak drive approximation is not applied. To do so, we solve the equations 9.2 for the self-consistent steady state solution. In doing so, we obtain a set of fifth degree polynomials in both σ_z and τ_z, which we solve numerically for the steady states for τ_z and σ_z. These solutions are then used to obtain the cavity steady state from which we find the reflection coefficient.

Figure 15, shows the reflection coefficient for the self-consistent steady state solution without the weak drive approximation for the same parameters as in figure 12. We observe the same pattern as with the external system in the ground state in the previously mentioned figure.

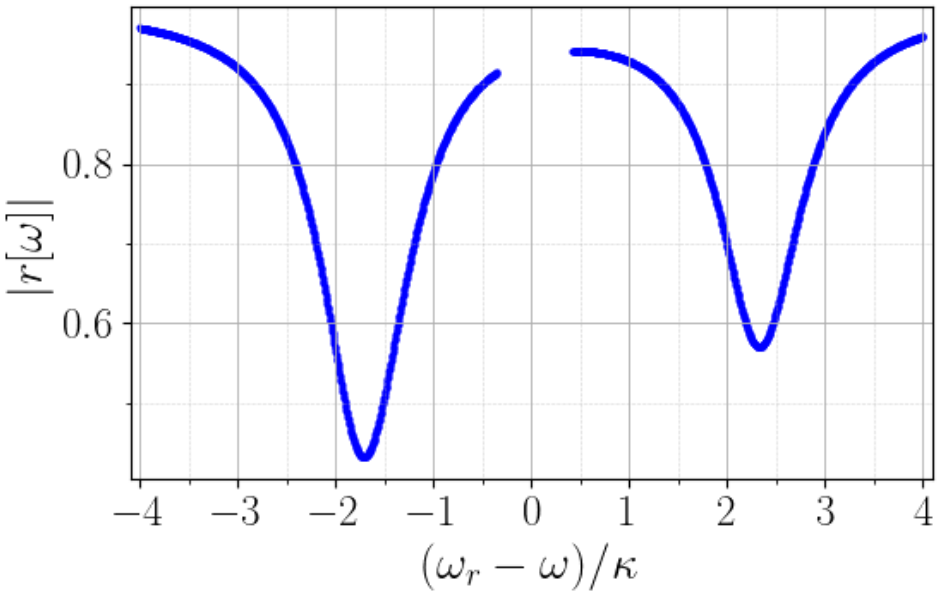

Figure 15: Reflection coefficient $r[\omega]$ as a function of probe frequency for the numerical steady state with an external DQD.
Parameters: $\omega_q = \omega_r$, $\omega_d = \omega_r + 2\kappa$, $g = 2\kappa$, $g_d = 0.5\kappa$, $\Gamma_\tau = \Gamma_\sigma = 1\kappa$, $\kappa_c = 0.5\kappa$.
The reflection in the steady state of the external system is unique and no longer a "function" of the state of the external system. The external system is now in a steady state according to its own equations of motion.

Since the problem is now solved numerically without the weak drive approximation, we can also look at the steady state solutions for the inversion operators τ_z and σ_z.

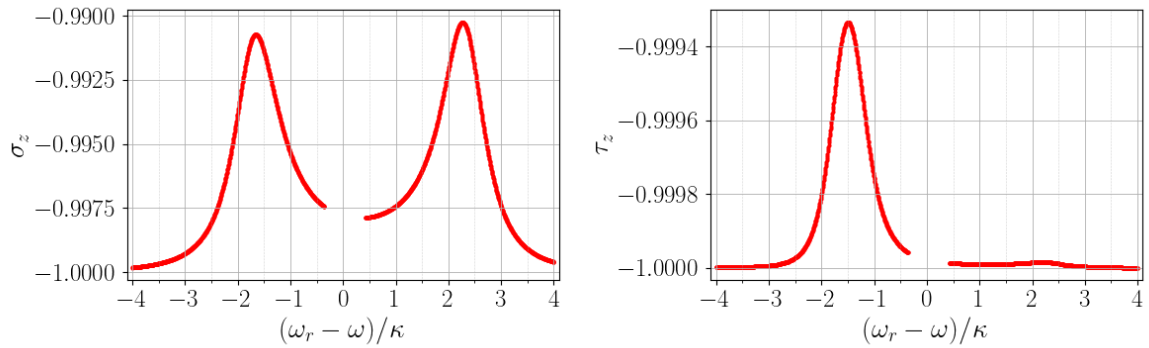

Figure 16: Inversion operators $\tau_z[\omega], \sigma_z[\omega]$ in the steady state, as a function of probe frequency. The x-axis shows the probe detuning relative to the cavity, and the y-axis shows the magnitudes of the inversion operators.
Parameters: $\omega_q = \omega_r$, $\omega_d = \omega_r + 2\kappa$, $g = 2\kappa$, $g_d = 0.5\kappa$, $\Gamma_\tau = \Gamma_\sigma = 1\kappa$, $\kappa_c = 0.5\kappa$.
The steady states of the inversion operators do not far exceed the ground state. The inversion operator of the external system has a peak at the resonance frequency of this system.

The magnitude of the steady states of the inversion operators are below zero for all probing frequencies, as seen in figure 16. It is also noticeable that neither operator deviates much from the ground state value, apart from at the resonance frequency.

If we push our model into the strongly coupled regime, and further into the dispersive regime, we also observe what seems to be a bistability, where there are several steady states for the same frequency. This can be seen in figure 17 and 18

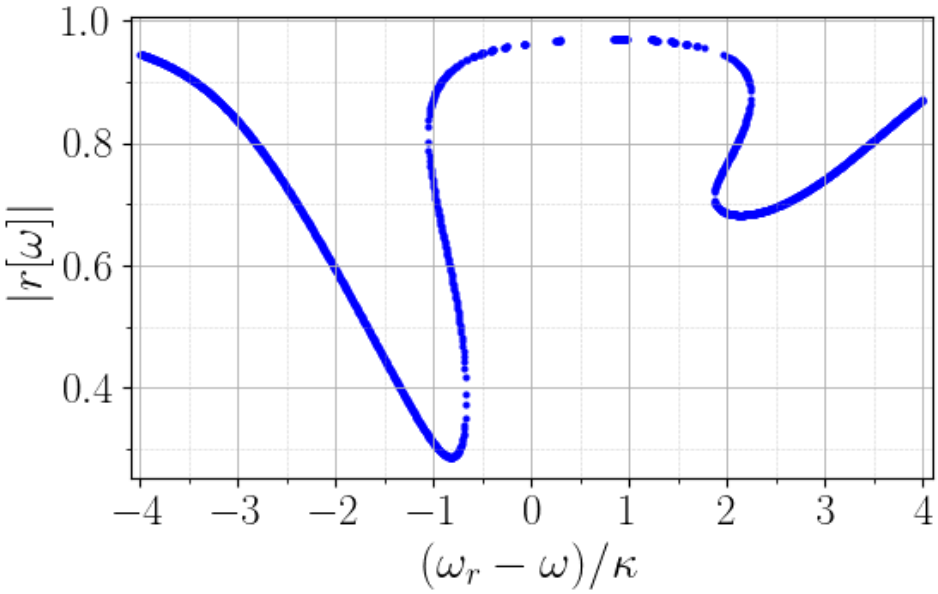

Figure 17: Reflection coefficient $r[\omega]$ as a function of probe frequency for the numerical steady state with an external quantum dot.
Parameters: $\omega_q = \omega_r + 3\kappa$, $\omega_d = \omega_r + 4$, $g_d = 2.5\kappa$,$g = 4\kappa$, $\Gamma_\tau = \Gamma_\sigma = 1\kappa$, $\kappa_c = 0.5$.
The reflection in the steady state of the external system is no longer unique. The reflection takes multiple values in some frequency ranges.

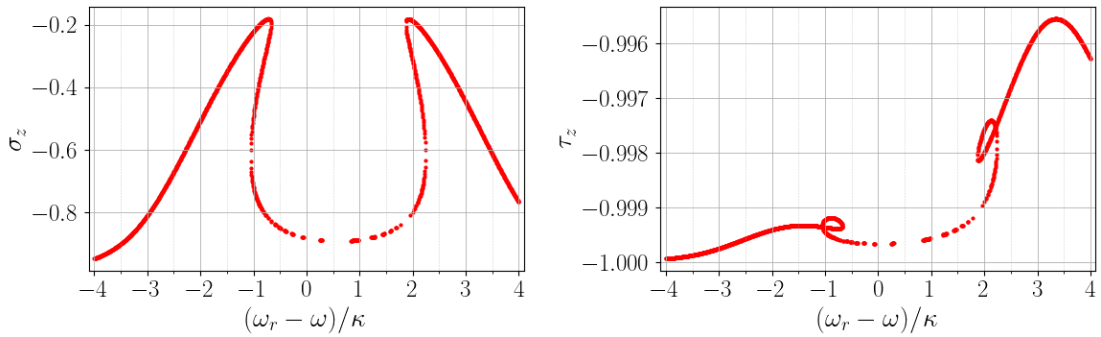

Figure 18: Inversion operators $\tau_z[\omega], \sigma_z[\omega]$ in the steady state, as a function of probe frequency. Parameters: $\omega_q = \omega_r + 3\kappa$, $\omega_d = \omega_r + 4$, $g_d = 2.5\kappa$,$g = 4\kappa$, $\Gamma_\tau = \Gamma_\sigma = 1\kappa$, $\kappa_c = 0.5$.
The steady states of the inversion operators significantly exceed the ground state. The steady state solutions are no longer unique, and takes multiple values in some frequency ranges. Note also that the inversion operator for the internal DQD, is far exceeding ground state.

This reflection behaves seemingly nonphysical, but it is not clear whether this apparent bistability is a physical result, or an effect of the mean-field approximation, and the investigation of this goes beyond the scope of this thesis. We can only state that the inversion operator for the internal DQD, significantly deviates from the ground state value. This violates the weak drive approximation $\sigma_z \approx -1$ and this is likely the cause of the bistability.

9.2.2 Fisher Information

Considering the same parameters as in the numerical solution in figure 15, but now in the weak drive approximation, in which we can work with the analytical expression for the steady state, we investigate the optimal range to probe the system at, in the same manner as in the case with the q-dot as an external system. To find the QFI for this system, we calculate the sensitivity to the state of the external system,

$$\left|\frac{\partial\langle a\rangle_{ss}}{\partial\tau_z}\right|^2 = \frac{4g_d^2 g^4 \sigma_z^2 \kappa_c |b_{in}|^2 \left|C - \frac{g_d\sigma_z S^2}{i\Gamma_\tau + 2\Delta_d + 4g_d\sigma_z C}\right|^2}{\left|-g^2\sigma_z + \left(i\Delta_r + \frac{\kappa}{2}\right)\left(-\frac{\Gamma_\sigma}{2} + 2ig_d\tau_z\left[C - \frac{g_d\sigma_z S^2}{i\Gamma_\tau + 2\Delta_d + 4g_d\sigma_z C}\right] + i\Delta_q\right)\right|^4}. \tag{9.29}$$

We now insert this into the equation for the QFI 7.6, to find

$$I_q = 4\kappa_c b_{in}^2 \left|\frac{\partial\langle a\rangle_{ss}}{\partial\langle\tau_z\rangle}\right|^2. \tag{9.30}$$

We now have an expression for the Fisher information consisting of all system parameters. Maximizing this expression yields the upper limit of the information that can be extracted by the measurement. We focus here on the probing frequency, and leave the other parameters as possible future work. This Fisher information is visualized for a range of probing frequencies below.

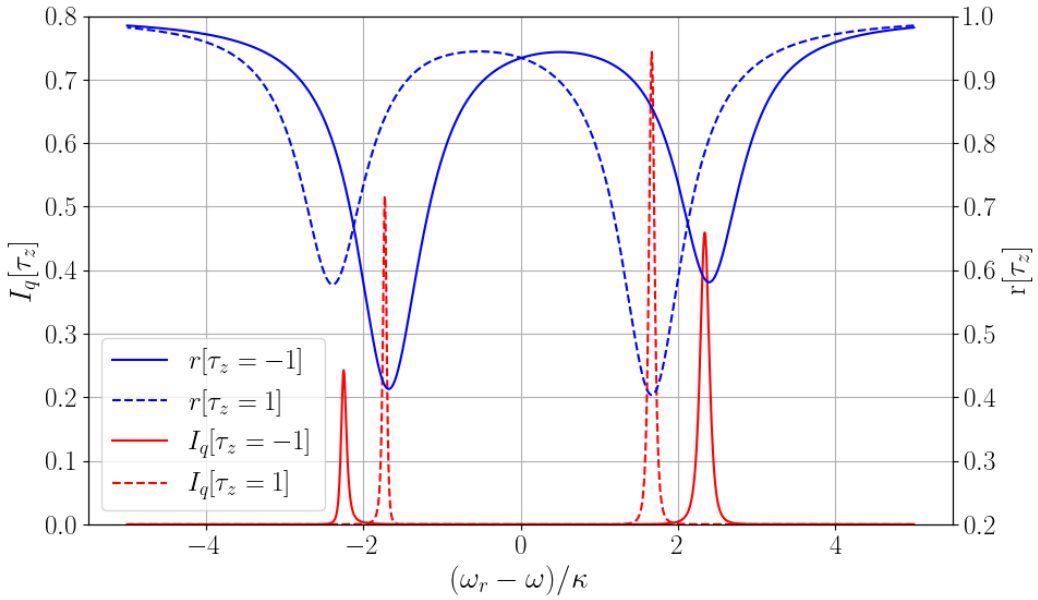

Figure 19: Reflection coefficient $r[\omega]$ (right), and the Fisher information $I_q[\omega]$ (left), as a function of probe frequency for the external qubit in the excited state (top) and ground state (bottom). Parameters: $\omega_q = \omega_r$, $\omega_d = \omega_r + 2\kappa$, $g = 2\kappa$, $g_d = 0.5\kappa$, $\Gamma_\tau = \Gamma_\sigma = 1$, $\kappa_c = 0.5$.
The QFI peaks around the point in the reflection with the greatest slope.

The optimal probing frequencies for this system with these parameters can be seen in figure 19. We note that the optimal probing frequency lies in the neighborhood of $\omega_r \pm g$, depending on the state of the external system. This should be compared to the variance in the signal, to see if this system can approach the Cramér-Rao bound, but this goes beyond the scope of this thesis, and the result taken from this analysis is simply the range at which maximal information gain can be achieved.

10 Discussion

In this work, we have investigated a hybrid quantum system in which a microwave resonator is coupled to a double quantum dot acting as a sensor, which is coupled to an additional external system whose state is to be inferred. The central objective has been to understand how the presence of this external system modifies the measurable properties of the cavity field, and how this modification can be used for indirect state discrimination.

A key result of this analysis is that the external system induces a state-dependent modification of the sensor qubit, which in turn affects the response of the cavity. In particular, the coupling leads to an effective shift in the qubit frequency, which propagates to the cavity through the light-matter interaction. As a result, the reflection coefficient gets a dependence on the state of the external system, resulting in shifts and distortions of the resonance features.

This behavior can be understood as a form of sensing, where the external system modifies the effective parameters of the sensor, rather than being measured directly. The cavity thus acts as an interface that converts microscopic changes in the system into measurable changes in the reflected microwave field.

10.1 Sensitivity and Fisher Information

To quantify the performance of this measurement scheme, we evaluated the Fisher information associated with the reflected signal. The results show that the sensitivity is maximized in regions where the reflection coefficient varies most rapidly with respect to the parameter of interest. In practice, this corresponds to probing frequencies near the steepest slopes of the resonance features. The QFI is also affected by the other system parameters, and should be maximized in all parameters within the limits set by an experimental setup for the most information possible extracted.

This highlights an important point for experimental implementations, optimal measurement is not achieved by maximizing signal amplitude, but by maximizing the response to small parameter changes. The Fisher information thus provides a useful criterion for selecting operating regime that enhance state distinguishability.

10.2 Comparison between External Systems

Two different models for the external system were considered, a single quantum dot with binary occupation, and a secondary two-level system. In the former case, the effect of the external system is primarily to introduce a shift in the resonance condition, leading to relatively simple modifications of the reflection spectrum. In the latter case, the dynamics become significantly richer, with additional coupling-induced features and more complex behaviour, but the spectral structures still show similar distortions of the reflection, due to the state of the external system. When considering a fully quantum external system, the possibility of having coherence adds new distinct physical behaviours. Instead of acting merely as a classical state switch that statically shifts the sensor qubit's detuning. This introduces coherent population oscillations, quantum back action, and hybridization between the sensor qubit and the external system. These quantum effects can manifest as distinct resonance features, interference in the reflection spectrum, and can either broaden or sharply narrow the reflection dips depending on the relative phase of the coupled dynamics.

While the two-level external system provides a more complete description of a realistic quantum device, it also introduces additional complexity, both analytically and numerically.

Nonetheless, in both cases the essential mechanism of indirect sensing via cavity response remains the same. In both cases, the state discrimination seems possible in both the resonant and dispersive regime. The resonant regime shows a greater reflection at nearly the same frequency, while the dispersive regime shows a clearer shift in the frequency at which the peaks appear at.

10.3 Limits of Approximations

Several approximations have been employed in this work. The rotating wave approximation and the Markov approximation are standard in the regime of weak coupling and near-resonant interactions, but may break down for stronger couplings or large detunings. The weak drive approximation simplifies the dynamics by assuming that the qubit remains close to its ground state, which is valid only when the drive strength is sufficiently small. An example of when this fails is figure 9, where the strong coupling violated the weak drive approximation and is the likely one cause of the bistability.

Most importantly, the use of a mean-field approximation to truncate the hierarchy of operator equations neglects correlations between subsystems. While this allows for analytical progress and efficient numerical solutions, it may fail to capture important quantum effects, particularly in regimes where entanglement or strong nonlinearities are present. Some observed features, such as bistability in the steady-state solutions, might be caused or influenced by this approximation.

10.4 Experimental Relevance

The system considered here is closely related to the setup in circuit quantum electrodynamics, used in the group of Ville Maisi, where quantum dots or superconducting qubits are coupled to microwave resonators. In this system, the reflection coefficient of the cavity can be measured, making it a practical observable for indirect state detection.

The results of this work suggest that coupling to an external system can be detected through shifts in the reflection spectrum, and that the sensitivity of this detection can be optimized by appropriate choice of probing frequency and system parameters. However, realistic implementations must also take into account decoherence, noise, and finite measurement resolution, which may reduce the achievable sensitivity.

11 Conclusion

In this work, we have investigated a hybrid quantum system in which a microwave resonator is coupled to a double quantum dot acting as a sensor, which in turn is coupled to an external quantum system whose state is to be inferred. Using input-output theory, we derived the reflection coefficient of the system and analyzed how it is modified by the presence and state of the external system. Furthermore, we quantified the sensitivity of this measurement scheme through the Fisher information associated with the reflected signal.

The results show that the external system induces measurable shifts and distortions in the cavity response, enabling indirect state discrimination. The sensitivity of this scheme was found to be maximized in regions where the reflection coefficient varies most rapidly with respect to the system parameters, rather than at resonance peaks. Additionally, the analysis revealed nonlinear effects and regimes in which the reflected signal show signs of bistability, indicating the complex interplay between coupling, dissipation, and driving and the possible breakdown of approximations.

The study relies on several simplifying approximations, including the rotating wave, Markov, weak drive, and mean-field approximations. While these make the analytical and numerical analysis more manageable, they may influence certain features of the results, such as the found bistability. A more complete treatment would therefore be required to fully assess these effects.

Overall, this work demonstrates how cavity-based measurements can be used as sensitive probes of coupled quantum systems, while also emphasizing the importance of carefully accounting for noise, correlations, and nonlinear dynamics in determining the ultimate measurement performance.

11.1 Outlook

There are several directions in which this work could be extended. A natural next step would be to go beyond the mean-field approximation and solve the full quantum master equation, allowing for a more accurate treatment of correlations and quantum effects. It would also be of interest to investigate the origin of the bistability in the reflection and determine whether it is purely an artifact of approximations, or if it persists in more complete models.

A more complete analysis would require explicit modeling of quantum noise in the output field, allowing for the calculation of the variance in the estimation of the external system's state. This would enable a direct comparison with the Cramér-Rao bound and provide insight into whether the measurement scheme operates near the quantum limit of sensitivity.

Further studies could explore optimization of the measurement protocol, for example by maximizing the Fisher information over a broader parameter space, or by considering alternative measurement strategies. Finally, extending the model to include more complex external systems or environments could provide a more realistic description of experimental conditions.

References

[1] A. Blais, R. Huang, A. Wallraff, S. M. Girvin, and R. J. Schoelkopf. Cavity quantum electrodynamics for superconducting electrical circuits: An architecture for quantum computation. *Phys. Rev. A*, 69:062320, Jun 2004.

[2] A. A. Clerk, M. H. Devoret, S. M. Girvin, F. Marquardt, and R. J. Schoelkopf. Introduction to quantum noise, measurement, and amplification. *Rev. Mod. Phys.*, 82:1155–1208, Apr 2010.

[3] A. Wallraff, D. Schuster, A. Blais, L. Frunzio, R. Huang, J. Majer, S. Kumar, S. Girvin, and R. Schoelkopf. Strong coupling of a single photon to a superconducting qubit using circuit quantum electrodynamics. *Nature*, 431:162–7, 10 2004.

[4] T. Frey, P. J. Leek, M. Beck, A. Blais, T. Ihn, K. Ensslin, and A. Wallraff. Dipole coupling of a double quantum dot to a microwave resonator. *Phys. Rev. Lett.*, 108:046807, Jan 2012.

[5] J. J. Viennot, M. C. Dartiailh, A. Cottet, and T. Kontos. Coherent coupling of a single spin to microwave cavity photons. *Science*, 349(6246):408–411, 2015.

[6] X. Mi, J. V. Cady, D. M. Zajac, P. W. Deelman, and J. R. Petta. Strong coupling of a single electron in silicon to a microwave photon. *Science*, 355(6321):156158, January 2017.

[7] J. Gambetta, A. Blais, M. Boissonneault, A. A. Houck, D. I. Schuster, and S. M. Girvin. Quantum trajectory approach to circuit qed: Quantum jumps and the zeno effect. *Phys. Rev. A*, 77:012112, Jan 2008.

[8] A. Blais, J. Gambetta, A. Wallraff, D. I. Schuster, S. M. Girvin, M. H. Devoret, and R. J. Schoelkopf. Quantum-information processing with circuit quantum electrodynamics. *Phys. Rev. A*, 75:032329, Mar 2007.

[9] S. L. Braunstein and C. M. Caves. Statistical distance and the geometry of quantum states. *Phys. Rev. Lett.*, 72:3439–3443, May 1994.

[10] V Giovannetti, S Lloyd, and L Maccone. Advances in quantum metrology. *Nature Photonics*, 5(4):222229, March 2011.

[11] V. B. Braginsky, F. Y. Khalili, and K. S. Thorne. *Quantum Measurement*. Cambridge University Press, 1992.

[12] V. B. Braginsky, Y. I. Vorontsov, and K. S. Thorne. Quantum nondemolition measurements. *Science*, 209(4456):547–557, 1980.

[13] G. Nogues, A. Rauschenbeutel, S. Osnaghi, M. Brune, J. Raimond, and S. Haroche. Seeing a single photon without destroying it. *Nature*, 400:239–242, 07 1999.

[14] E.T. Jaynes and F Cummings. Comparison of quantum and semiclassical radiation theories with application to the beam maser. *Proceedings of the IEEE*, 51:89 – 109, 02 1963.

[15] S. Andersson and F. Omlor. Introduction to input–output theory. Lecture notes, May 2025.

[16] C. W. Gardiner and M. J. Collett. Input and output in damped quantum systems: Quantum stochastic differential equations and the master equation. *Phys. Rev. A*, 31:3761–3774, Jun 1985.

[17] K. Fujii. Introduction to the rotating wave approximation (rwa): Two coherent oscillations. *Journal of Modern Physics*, 08(12):2042–2058, 2017.

[18] S. M. Kay. *Fundamentals of Statistical Signal Processing: Estimation Theory*. Pearson, 1993.

[19] G. Toth and I. Apellaniz. Quantum metrology from a quantum information science perspective. *JOURNAL OF PHYSICS A-MATHEMATICAL AND THEORETICAL*, 47(42, SI), OCT 24 2014.

[20] C. W. Helstrom. Viii quantum estimation theory. In *Quantum Detection and Estimation Theory*, volume 123 of *Mathematics in Science and Engineering*, pages 235–293. Elsevier, 1976.